Hypoxia Alters Corneal Circadian Rhythms and Disrupts Epithelial, Neural, and Immune Balance

Jiangman Liu,[1–4] Yuxin Jing,[5,6] Jiaxin Wu,[5,6] Dingli Lu,[1–3] and Zhijie Li[1–3]

[1]Henan Key Laboratory of Ophthalmology & Visual Science, Henan Eye Hospital, Henan Provincial People's Hospital, Zhengzhou, Henan, China
[2]People's Hospital of Zhengzhou University, Zhengzhou, Henan, China
[3]People's Hospital of Henan University, Zhengzhou, Henan, China
[4]Department of Pathology, School of Medicine, Jinan University, Guangzhou, Guangdong, China
[5]International Ocular Surface Research Center, Institute of Ophthalmology, and Key Laboratory for Regenerative Medicine, School of Medicine, Jinan University, Guangzhou, Guangdong, China
[6]Department of Ophthalmology, The First Affiliated Hospital of Jinan University, Guangzhou, Guangdong, China

Correspondence: Zhijie Li, Henan Key Laboratory of Ophthalmology & Visual Science, Henan Eye Hospital, Henan Provincial People's Hospital, 7 Weiwu Rd., Zhengzhou 450003, China;
tzhijieli@jnu.edu.cn,
zhijielee@vip.163.com.

Received: July 22, 2025
Accepted: September 25, 2025
Published: November 4, 2025

Citation: Liu J, Jing Y, Wu J, Lu D, Li Z. Hypoxia alters corneal circadian rhythms and disrupts epithelial, neural, and immune balance. *Invest Ophthalmol Vis Sci.* 2025;66(14):5. https://doi.org/10.1167/iovs.66.14.5

Purpose. The cornea operates under robust circadian control and is essential for ocular-surface homeostasis. Hypoxic stress—prevalent in many eye disorders and systemic conditions—can disturb these rhythms and compromise epithelial, neural, and immune balance. Here, we examine how environmental hypoxia (EH) and chemical hypoxia (CH) reshape corneal clock-gene expression and tissue integrity.

Methods. Male C57BL/6J mice were exposed to normoxia (NC), EH (10% O_2), or CH ($CoCl_2$, 15 mg/kg/d intraperitoneally) for 14 days. Corneas were collected at 3-hour intervals across a 24-hour cycle for bulk RNA sequencing. Rhythmic genes were identified by Jonckheere–Terpstra–Kendall CYCLE (JTK_CYCLE), and pathway enrichment was assessed using Gene Set Enrichment Analysis (GSEA) and Phase Set Enrichment Analysis (PSEA). Immunofluorescence staining evaluated epithelial junction proteins (ZO-1 and occludin), neural markers (βIII-tubulin), and immune cells (Ly6G$^+$ neutrophils, $\gamma\delta$ T cells).

Results. Hypoxia significantly increased rhythmic transcripts (by ~43% in EH and ~35% in CH), with over 65% of rhythmic genes showing phase shifts. CH specifically upregulated core circadian clock genes (*Per1*, *Cry2*, *Nr1d2*, *Rora*) and downregulated *Per2*, possibly via *HIF-1α*–mediated mechanisms. Both EH and CH impaired epithelial barrier integrity, reduced corneal nerve density, and altered immune cell infiltration, with peak disruption at Zeitgeber time 18 (ZT18). Additionally, CH uniquely induced barrier dysfunction and immune suppression at ZT3, indicating a model-specific vulnerability window.

Conclusions. Hypoxia drives model-specific and circadian phase-dependent reprogramming of corneal transcriptomic rhythms, resulting in coordinated structural and immune dysfunction. Identifying ZT18 and ZT3 as critical phases highlights the potential for chronotherapeutic interventions in hypoxia-related ocular surface disorders.

Keywords: hypoxia, circadian rhythm, cornea, transcriptomics, epithelial barrier, tight junctions, innate immunity

The cornea is a transparent, avascular tissue that forms the primary refractive interface of the eye and is indispensable for high-acuity vision. Its physiological stability depends on stromal transparency, endothelial ion transport, and a finely tuned immune-privileged milieu.[1,2] Disruption of any of these homeostatic elements compromises visual function and destabilizes the ocular surface.[1]

Hypoxia is a frequent and clinically significant stressor in corneal biology, arising from extended wear of low-oxygen-permeable contact lenses, nocturnal eyelid closure, high-altitude exposure, and systemic disorders such as chronic obstructive pulmonary disease and obstructive sleep apnea (OSA).[3–5] These insults are linked to delayed epithelial turnover, corneal edema, reduced corneal sensitivity, and chronic inflammation—hallmarks of ocular-surface dysfunction.[3,6]

Although the phenotypic sequelae of corneal hypoxia are well documented, the underlying molecular mechanisms—especially those involving transcriptional and temporal regulation—remain incompletely understood. Growing evidence indicates that the circadian clock, a cellular time-

keeping system that orchestrates ~24-hour gene-expression rhythms, strongly modulates tissue responses to stress.[7,8] In the cornea, circadian regulation controls epithelial renewal, and wound repair.[9]

This local clockwork operates through transcription–translation feedback loops driven by core regulators (*BMAL1*, *CLOCK*, *PER*, *CRY*) and nuclear receptors (*NR1D1*/2, *RORs*).[10] Genetic or environmental clock disruption impairs epithelial integrity, neural regeneration, and immune balance in the cornea, yet the impact of hypoxia on these pathways has not been systematically explored. Notably, hypoxic exposures—such as those in OSA or overnight lens wear—follow daily patterns, suggesting crosstalk between hypoxic signaling and circadian control.[6,7] Recent studies demonstrating bidirectional regulation between hypoxia-inducible factor-1α (*HIF-1α*) and the clock component *BMAL1* further support this interaction.[8,11]

However, no investigation has yet mapped how distinct forms of hypoxia reshape corneal circadian transcriptional dynamics across an entire light–dark cycle. In particular, it remains unclear whether environmental hypoxia (EH) and chemical hypoxia (CH) elicit phase-specific effects on epithelial, neural, and immune regulation.

To address this gap, we interrogated how EH and CH reprogram the corneal circadian transcriptome using high-resolution time-series RNA sequencing (RNA-seq). We hypothesized that the two hypoxia paradigms disrupt local clock-gene expression via distinct mechanisms, yielding temporally divergent patterns of tissue dysfunction: EH would primarily perturb neuroimmune rhythmicity around Zeitgeber time 18 (ZT18), whereas CH would induce immunosuppressive effects peaking at ZT3. Through integrative transcriptomic and functional analyses, we sought to (1) define the molecular architecture of hypoxia-induced circadian disruption, (2) delineate model-specific effects on corneal structure and immunity, and (3) identify circadian phases of vulnerability with therapeutic relevance for hypoxia-associated ocular-surface disease.

Materials and Methods

Experimental Workflow and Circadian Sampling

Male specific-pathogen-free (SPF) C57BL/6J mice (10 weeks old) were randomly assigned to three experimental groups: normoxia (NC), EH, and CH (Fig. 1A). After a 2-week period of circadian entrainment, mice were exposed to the respective experimental conditions for 14 consecutive days. Corneal tissues were collected on day 14 at eight ZT points (ZT0, ZT3, ZT6, ZT9, ZT12, ZT15, ZT18, and ZT21; $n = 3$ mice/group/time point) (Fig. 1B).[12]

Collected samples underwent downstream analyses: (1) bulk RNA-seq to identify circadian rhythmicity using Jonckheere–Terpstra–Kendall CYCLE (JTK_CYCLE), with functional annotations performed via Gene Set Enrichment Analysis (GSEA) and Phase Set Enrichment Analysis (PSEA)[13–15]; (2) time-series clustering of rhythmic genes using fuzzy C-means clustering algorithms (Mfuzz) and the Kyoto Encyclopedia of Genes and Genomes (KEGG) (Fig. 1C)[16,17]; and (3) immunofluorescence staining to assess epithelial (zonula occludens-1 [ZO-1], occludin), neural (βIII-tubulin), and immune (Ly6G neutrophils, $\gamma\delta$ T cells) markers. Imaging and quantitative analysis followed standardized protocols to ensure consistency (Fig. 1D).[18–23]

Animals and Ethical Approval

Male SPF C57BL/6J mice (10 weeks old) were purchased from GemPharmatech LLC (Nanjing, China). Animals were housed under SPF conditions with controlled temperature, humidity, and a strict 12-hour light/dark cycle (lights on at 07:00, ZT0; lights off at 19:00, ZT12), with free access to food and water. All experimental procedures adhered to the ARVO Statement for the Use of Animals in Ophthalmic and Vision Research and were approved by the Institutional Animal Care and Use Committee of Henan Provincial People's Hospital (Approval No. HNEECA 81470603).

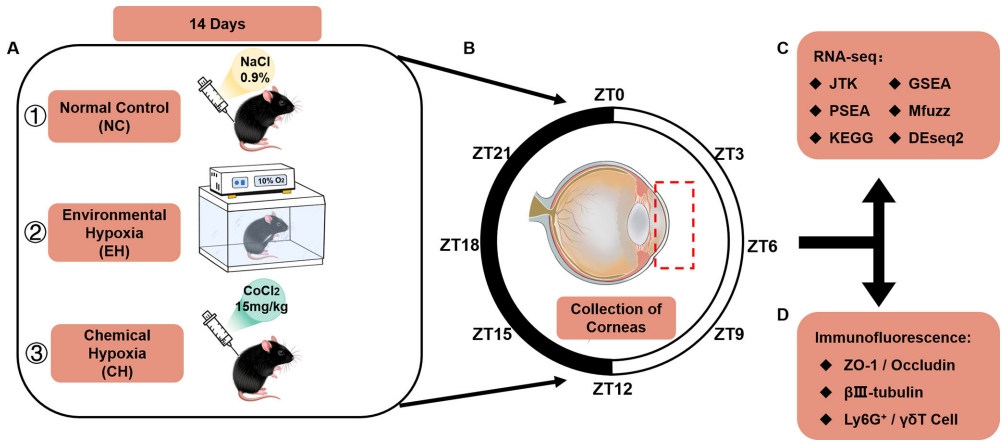

Figure 1. Experimental workflow and circadian sampling strategy, with a schematic overview of the in vivo experimental design. (**A**) Male C57BL/6J mice were assigned to three groups: NC (NaCl 0.9%, intraperitoneally, 21% O_2, for 14 days), EH (10% O_2 for 14 days), and CH (cobalt chloride, 15 mg/kg/d, intraperitoneally, for 14 days). All mice were maintained under a 12:12 light–dark cycle (lights on at ZT0 = 07:00; lights off at ZT12 = 19:00) for circadian entrainment. (**B**) Corneal tissues were collected at eight ZT points (ZT0 to ZT21, every 3 hours; $n = 3$ mice per group per time point). (**C**, **D**) Downstream analyses included bulk RNA-seq (for JTK_CYCLE rhythmicity detection, GSEA, and PSEA), time-series clustering (Mfuzz), gene function analysis (KEGG), differential gene expression analysis (DESeq2), and immunofluorescence (IF) for epithelial, neural, and immune markers (ZO-1, βIII-tubulin, Ly6G, and $\gamma\delta$ T cells).

Investigative Ophthalmology & Visual Science

Hypoxia Models

Mice were randomly assigned into three experimental conditions: NC, EH, and CH. The NC group was maintained in ambient air (21% O_2) and received daily intraperitoneal injections of 0.9% NaCl solution as vehicle control. For the EH condition, mice were housed within a sealed hypoxic chamber continuously supplied with a gas mixture of 10% O_2 balanced with 90% N_2 for 14 consecutive days. Oxygen levels and gas flow (0.1–0.2 L/min) were continuously monitored and adjusted using an inline oxygen analyzer (Engineered Systems & Designs, Wilmington, DE, USA) to maintain stable hypoxic conditions.[24] In the CH condition, mice received daily intraperitoneal injections of cobalt chloride ($CoCl_2$, 15 mg/kg/d; Sigma-Aldrich, St. Louis, MO, USA) for 14 days. $CoCl_2$ treatment chemically stabilizes *HIF-1α*, simulating sustained intracellular hypoxic signaling.[24,25] These two hypoxic models allowed comparative investigation of distinct physiological and cellular hypoxic responses, specifically their impacts on corneal circadian gene regulation and tissue homeostasis.

Corneal Immunofluorescence Staining and Quantitative Analysis

To evaluate the structural and immune effects of hypoxic stress on the cornea, whole-mount immunofluorescence staining was performed on freshly dissected mouse corneas. Immediately after enucleation, tissues were fixed in 4% paraformaldehyde for 30 minutes at room temperature, followed by thorough washes in phosphate-buffered saline (PBS). Samples were then permeabilized and blocked overnight at 4°C in 0.1% Triton X-100 (93443; Sigma-Aldrich) supplemented with 2% bovine serum albumin to minimize nonspecific binding.[19–21,23]

For visualization of epithelial tight junctions, tissues were incubated with fluorescein isothiocyanate (FITC)-conjugated rabbit anti-mouse ZO-1 (CL488-21773; Proteintech, Rosemont, IL, USA) and phycoerythrin (PE)-conjugated rabbit anti-mouse occludin (CL594-13409; Proteintech). Corneal nerves were labeled using a rat anti-mouse βIII-tubulin antibody (AB15708A4; Sigma-Aldrich). Immune cells were identified using a FITC-labeled rat anti-mouse Ly6G antibody (551460; BD Biosciences, Franklin Lakes, NJ, USA) and T-cell receptor γ antibody conjugated with PE (553178, GL3 clone; BD Biosciences).[23,26,27]

Stained tissues were mounted in antifade medium and imaged using the DeltaVision Elite imaging system (GE Healthcare Life Sciences, Chicago, IL, USA) under standardized exposure parameters. Image acquisition settings were kept constant across experimental groups to allow for valid quantitative comparisons. Quantitative image analysis was conducted using ImageJ (National Institutes of Health, Bethesda, MD, USA), including measurements of tight junction continuity, nerve fiber density, and immune cell abundance. All image processing and data extraction were performed in a blinded manner to eliminate observer bias.[21,28]

Central Corneal Thickness Measurement

Central corneal thickness (CCT) was measured using optical coherence tomography (OCT; YG-20W Pro; TowardPi, Beijing, China). Mice were gently secured on a customized ophthalmic platform to ensure ocular stability and accurate positioning during imaging. Prior to scanning, one or two drops of sterile PBS were applied with a micropipette to both eyes to remove any debris or secretions. One drop of artificial tears was then instilled to maintain adequate corneal hydration and smoothness throughout the imaging process, thereby ensuring high-quality OCT images. The head position of each mouse was carefully adjusted so that the cornea was aligned perpendicularly to the scanning probe. Using the fixation-light guidance system of the device under real-time imaging preview, the central cornea (pupillary center) was positioned precisely at the center of the scanning field. For each eye, the final CCT value was calculated as the mean of three valid consecutive scans.

Corneal Permeability Assay

A 1% sodium fluorescein solution was instilled into the conjunctival sac of each mouse eye, followed by gentle eyelid closure to ensure uniform distribution of the dye across the corneal surface. After 90 seconds, the ocular surface was rinsed thoroughly with physiological saline, and excess fluid around the eye was carefully blotted. Corneal staining was then examined under cobalt blue light using a slit-lamp biomicroscope, and the extent of fluorescein uptake was documented.[9]

Corneal Sensitivity Assessment

Mechanical sensitivity of the cornea was assessed using a Cochet–Bonnet esthesiometer (8630-1490-29; Visionix, Pont-de-l'Arche, France) in accordance with a previously validated protocol.[21] Mice were evaluated without the use of anesthesia and gently restrained by cervical traction to minimize movement while maintaining physiological responsiveness. The nylon monofilament of the esthesiometer was applied perpendicularly to four quadrants of the central cornea. Testing began at the maximum filament length of 6.0 cm and was sequentially reduced by 0.5-cm increments until 0.5 cm, ensuring adequate contact and stimulus consistency. Each filament length was tested four times per site. A blink reflex in response to the filament touch was recorded as a positive response. Absence of a blink at a given length was classified as a negative response. If no blink response was elicited even at the shortest filament length (0.5 cm), a corneal sensitivity score of 0 was assigned, indicating complete sensory loss. All sensitivity measurements were performed by a single examiner blinded to group allocation to prevent assessment bias. This approach ensured consistent evaluation across experimental groups and preserved the integrity of quantitative sensory data.[29]

Collection and Total RNA Extraction

To assess circadian transcriptomic alterations under hypoxic stress, corneal tissues were collected from NC, EH, and CH groups across an entire 24-hour circadian cycle. Mice were maintained under a strict 12-hour light/12-hour dark regimen and euthanized at 3-hour intervals corresponding to ZT points ZT0, ZT3, ZT6, ZT9, ZT12, ZT15, ZT18, and ZT21 ($n = 3$ mice per group per time point). Immediately following euthanasia, bilateral corneas were excised and snap-frozen in liquid nitrogen to preserve RNA integrity.[12,30]

Total RNA was extracted using the RNeasy Mini Kit (QIAGEN, Hilden, Germany) according to the manufacturer's protocol. This included mechanical tissue homoge-

nization, on-column DNase I digestion to eliminate genomic DNA contamination, and elution in RNase-free water. RNA concentration and purity were assessed using a NanoDrop 2000 spectrophotometer (Thermo Fisher Scientific, Waltham, MA, USA), and RNA integrity was evaluated with the Agilent 2100 Bioanalyzer (Agilent Technologies, Santa Clara, CA, USA). Only samples with RNA integrity numbers (RINs) > 8.0 were deemed suitable for downstream sequencing analysis. To avoid light-induced transcriptional artifacts during dark-phase sample collection (ZT12–ZT21), all procedures were carried out under dim red light (3 W, DG-20A; Hengshuo Instruments, Zhejiang, China), following established protocols for circadian time-point tissue harvesting.

Library Preparation and RNA Sequencing

The quality of total RNA was assessed using a NanoDrop 2000 spectrophotometer) and an Agilent 2100 Bioanalyzer. All samples exhibited RINs between 8.1 and 9.0 and 28S/18S ribosomal RNA (rRNA) ratios ranging from 1.1 to 1.4, meeting the criteria for high-throughput transcriptome sequencing.[31] Messenger RNA (mRNA) was isolated from total RNA using Dynabeads Oligo(dT) magnetic beads (Thermo Fisher Scientific), followed by chemical fragmentation to produce short RNA fragments. First-strand complementary DNA (cDNA) synthesis was performed using random hexamer primers, and second-strand synthesis was completed following enzymatic degradation of the RNA template. The resulting double-stranded cDNA was end repaired, A tailed, and ligated to sequencing adapters containing unique index barcodes.

The ligated products were purified using AMPure XP magnetic beads (Beckman Coulter, Brea, CA, USA), amplified via polymerase chain reaction (PCR), and subjected to a second round of purification to remove adapter dimers and low-molecular-weight fragments. Final library quality and insert size distribution were verified using the Agilent 2100 Bioanalyzer.

Qualified libraries were circularized into DNA nanoballs through bridge ligation and amplified using phi29 DNA polymerase. Sequencing was performed on the BGISEQ-500 platform (BGI Group, Shenzhen, China) with a single-end 50-bp read configuration (SE50), targeting a sequencing depth of ~20 million reads per sample.

Raw sequencing reads were processed using SOAPnuke 1.5.2 to remove adapter sequences, filter out low-quality reads ($Q < 20$), and eliminate rRNA contamination. Clean reads were aligned to the mouse reference genome (GRCm38.p6, National Center for Biotechnology Information [NCBI] GCF_000001635.26) using HISAT2 2.0.4 and Bowtie2 2.2.5. Gene-level quantification was carried out with RSEM 1.2.8, and all libraries achieved alignment rates exceeding 90%.[31–33]

Quantitative Real-Time Polymerase Chain Reaction

Total RNA was extracted from frozen corneal tissues using the Total RNA Extractor (TRIzol) Kit (B511311; Sangon Biotechnology, Shanghai, China) according to the manufacturer's instructions. The integrity and concentration of the isolated RNA were assessed prior to downstream applications. cDNA was synthesized using the Maxima Reverse Transcriptase Kit (EP0743; Thermo Fisher Scientific). Quantitative real-time polymerase chain reaction (RT-qPCR) was performed with the SGExcel FastSYBR Mixture Kit (B532955; Sangon Biotechnology), following the manufacturer's protocol. Glyceraldehyde 3-phosphate dehydrogenase (GAPDH) was used as the internal control, and relative gene expression levels were calculated using the comparative Ct ($\Delta\Delta$Ct) method ($2^{-\Delta\Delta Ct}$). Primer sequences are provided in Supplementary Table S1.

Circadian Gene Analysis

Circadian transcriptional rhythms in corneal tissue were analyzed using the JTK_CYCLE algorithm (version 3), a nonparametric method based on the Jonckheere–Terpstra–Kendall test, implemented in R (R Foundation for Statistical Computing, Vienna, Austria).[13,34,35] Prior to rhythm detection, RNA-seq data were normalized, and transcripts with low expression (fragments per kilobase of transcript per million mapped reads [FPKM] ≤ 0.1 across all time points) were excluded to improve signal robustness. Genes exhibiting statistically significant rhythmic expression were identified using a Bonferroni-adjusted P value (P_adj) < 0.01 threshold, and non-rhythmic genes were defined as those with P_adj ≥ 0.01.

For each rhythmic gene, the peak expression phase (ZT of maximal expression) and amplitude (range of oscillation) were computed to characterize its temporal profile. To explore temporal structure among rhythmic transcripts, phase-based clustering was conducted using the K-means algorithm, grouping genes by peak phase across the 24-hour circadian cycle.

Circadian dynamics were visualized using a suite of R-based tools including ggplot2. Outputs included global heatmaps of rhythmic gene expression, circular rose plots summarizing phase distribution, and representative line plots of prototypical oscillatory patterns. These analyses provided a high-resolution temporal map of the corneal circadian transcriptome and enabled direct comparison of rhythmic architecture across normoxic and hypoxic conditions.

Differential Gene Expression

To identify genes associated with corneal epithelial barrier, neural, and immune pathways, we utilized the KEGG (https://www.genome.jp/kegg/) and GeneCards (https://www.genecards.org/) databases. Differential expression analysis was performed using the DESeq2 package in R 1.32.0 (https://bioconductor.org/packages/release/bioc/html/DESeq2.html), which applies a negative binomial distribution to compute $\log_2$ fold change (FC) and P value. P values were adjusted using the Benjamini–Hochberg method. Genes with P_adj < 0.05 and $|\log_2 FC| > 0.585$ were classified as differentially expressed genes (DEGs).

Functional Annotation and Pathway Enrichment Analysis

To investigate the biological functions and temporal dynamics of circadian-regulated genes, we performed integrative pathway enrichment analyses using KEGG, PSEA, and GSEA. KEGG annotation was conducted by aligning gene sequences against the KEGG and NCBI RefSeq databases using BLASTALL (NCBI). Pathway enrichment was evaluated

Investigative Ophthalmology & Visual Science

using Fisher's exact test with multiple testing correction via the Benjamini–Hochberg procedure. Pathways with adjusted Q values < 0.05 were considered statistically significant.

Gene Ontology (GO) analysis was conducted to investigate the molecular functions, cellular components, and biological processes associated with the identified genes. Candidate genes were mapped to corresponding terms in the GO database (http://www.geneontology.org), and the number of genes assigned to each term was calculated. Statistical significance was determined using a Benjamini–Hochberg multiple-testing correction, with the adjusted P value (Q value) threshold set at <0.05.

PSEA was used to assess phase-dependent pathway regulation. PSEA 1.1 was conducted using KEGG genesets from the Molecular Signatures Database (MSigDB). Genes were binned by circadian peak phase (0–24 hours) based on rhythmic expression profiles, and enrichment was calculated using Kuiper's test. Genesets containing between 5 and 5000 genes were included in the analysis, with significance set at $Q < 0.05$. Results were visualized as circular (polar) plots to illustrate temporal distribution.

GSEA 3.0 was employed to identify condition-specific pathway activation in NC, EH, and CH groups. Analyses were performed using curated genesets from MSigDB (c2.cp.kegg.v7.2). Pathways were ranked based on the normalized enrichment score (NES), and significance was defined as a false discovery rate (FDR) < 0.25 after Benjamini–Hochberg correction. Enrichment results were presented using ranked enrichment plots and summary bar graphs.

Time-Series Clustering of Circadian Gene Expression

To characterize the temporal expression dynamics of circadian transcripts over a 24-hour cycle, we performed time-series clustering using the fuzzy C-means algorithm implemented in the R package Mfuzz. Genes identified as rhythmic by JTK_CYCLE (P_adj < 0.01) were subjected to Z-score normalization to account for baseline expression differences across time points. Genes with minimal temporal variation (defined as FC < 1.5 across all time points) were excluded to improve clustering resolution. The fuzzifier parameter was set to 1.0 to balance between intra-cluster tightness and inter-cluster overlap. The optimal number of clusters ($C = 3$–6) was determined based on cluster validity indices, including the Dunn and Xie–Beni criteria. Clustering iterations were performed up to 1000 times with a convergence threshold of $1e^{-6}$. Cluster-specific temporal expression patterns were visualized using ggplot2 as average expression trajectories, with corresponding heatmaps generated to represent individual gene dynamics across ZT points. Functional annotation of each cluster was conducted through KEGG pathway enrichment analysis, allowing interpretation of phase-specific transcriptional modules related to circadian regulation and hypoxia-responsive signaling.

Statistical Analysis

All statistical analyses were performed using Prism 9.0 (GraphPad Software, Boston, MA, USA). Data distributions were tested for normality using the Shapiro–Wilk test. For comparisons involving normally distributed data, two-tailed unpaired Student's t tests were applied, followed by Bonferroni correction for multiple comparisons where applicable. For non-normally distributed data, the Mann–Whitney U test was used. Quantitative data are reported as mean ± standard deviation (SD), and statistical significance was defined as $P < 0.05$. For transcriptomic analyses, heatmaps representing circadian gene expression profiles were generated using the pheatmap package in R. Gene set overlaps were visualized using Venn diagrams constructed in Venny 2.1.0 (https://bioinfogp.cnb.csic.es/tools/venny/).

Results

Circadian Rhythmicity Is Extensively Reprogrammed in the Cornea Under Environmental and Chemical Hypoxia

To investigate the impact of hypoxia on circadian gene expression in the cornea, we performed high-resolution time-series bulk RNA-seq across eight ZT points (ZT0–ZT21) in mice subjected to NC, EH, or CH. Among the 19,333 expressed transcripts (FPKM > 0.1), 2545 genes (13.2%) exhibited significant rhythmicity under NC conditions, as determined by JTK_CYCLE analysis. Both EH and CH led to an increased number of rhythmic transcripts, with 3645 (18.9%) and 3438 (17.8%) rhythmic genes identified, respectively (P_adj < 0.01) (Fig. 2A; Supplementary Table S2).

Despite the overall increase in rhythmic gene number, hypoxia induced substantial changes in the composition of the rhythmic transcriptome. In the EH group, 1462 rhythmic genes were shared with NC, whereas 1083 genes lost rhythmicity and 2183 genes became newly rhythmic (Figs. 2B–E). Similarly, in the CH group, 1269 genes overlapped with NC, and 1276 lost rhythmicity and 2169 gained rhythmicity (Figs. 2B, 2F–H), indicating a dynamic turnover of rhythmic gene sets under both hypoxic conditions.

We next assessed whether hypoxia altered the phase of rhythmic gene expression. In EH, 964 of 1462 shared rhythmic genes (65.94%) exhibited phase shifts, with 67.12% showing phase advances and 32.88% delays (Fig. 2I). In the CH group, a comparable proportion of phase-shifted genes was observed (832/1269; 65.56%), but with a reversed trend, where 66.59% of genes were phase delayed (Fig. 2J). The average peak phase shifted from ZT22.8 in NC to ZT3.4 in EH, as shown by rose plot analysis (Figs. 2K, 2L). CH-specific rhythmic genes exhibited a narrow peak phase distribution centered around the dark–light transition (ZT0.4), contrasting with the broader phase dispersion seen in NC (Figs. 2M, 2N). These results indicate that both EH and CH remodel the circadian transcriptome of the cornea, with distinct effects on rhythmic gene number, composition, and phase architecture.

Hypoxia Induces Phase-Specific Functional Reprogramming of Circadian Genes in the Cornea

To evaluate the circadian phase structure of biological processes modulated by hypoxia, we performed PSEA on rhythmic genes uniquely identified under NC, EH, and CH conditions. Temporal enrichment profiles were visualized as rose plots using KEGG pathway annotations. In NC samples, rhythmic genes exhibited a broad phase distribution, with a peak in pathway enrichment occurring near the end of the dark phase (ZT22.8) (Fig. 3A). In EH-exposed corneas, rhythmic gene enrichment shifted toward earlier time points,

Investigative Ophthalmology & Visual Science

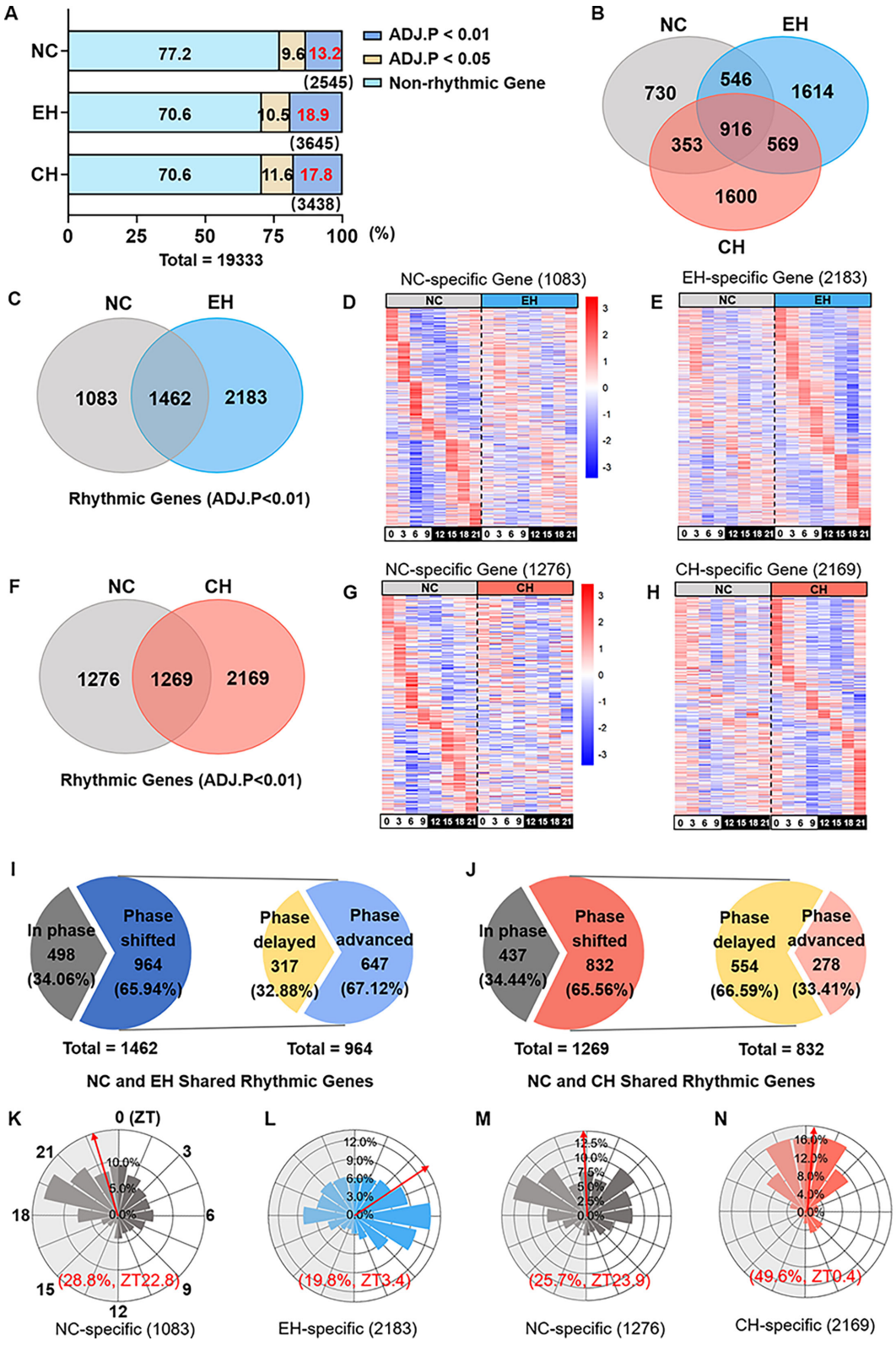

Figure 2. Circadian transcriptome reprogramming in the mouse cornea under EH and CH. (**A**) Proportion of rhythmic transcripts (adjusted $P < 0.01$, identified using JTK_CYCLE) in the cornea under NC, EH, and CH conditions. (**B**) Three-way Venn diagram showing rhythmic gene overlap across NC (*gray*), EH (*blue*), and CH (*red*) groups. (**C–E**) Differences in rhythmic genes (**C**) and expression heatmaps (**D**, **E**) between the NC and EH groups at eight circadian time points. (**F–H**) Differences in rhythmic genes (**F**) and expression heatmaps (**G**, **H**) between the NC and CH groups at eight circadian time points. (**I**, **J**) Pie chart showing the proportion of phase-shifted and unshifted genes shared between NC and EH (**I**), as well as between the NC and CH (**J**). (**K–N**) Rose plot of peak expression phases of NC-specific and EH-specific rhythmic genes (**K**, **L**), as well as NC-specific and CH-specific rhythmic genes (**M**, **N**). In the rose plots, *red arrows* indicate the mean phase vector and *shaded areas* denote the dark phase (ZT12–ZT24).

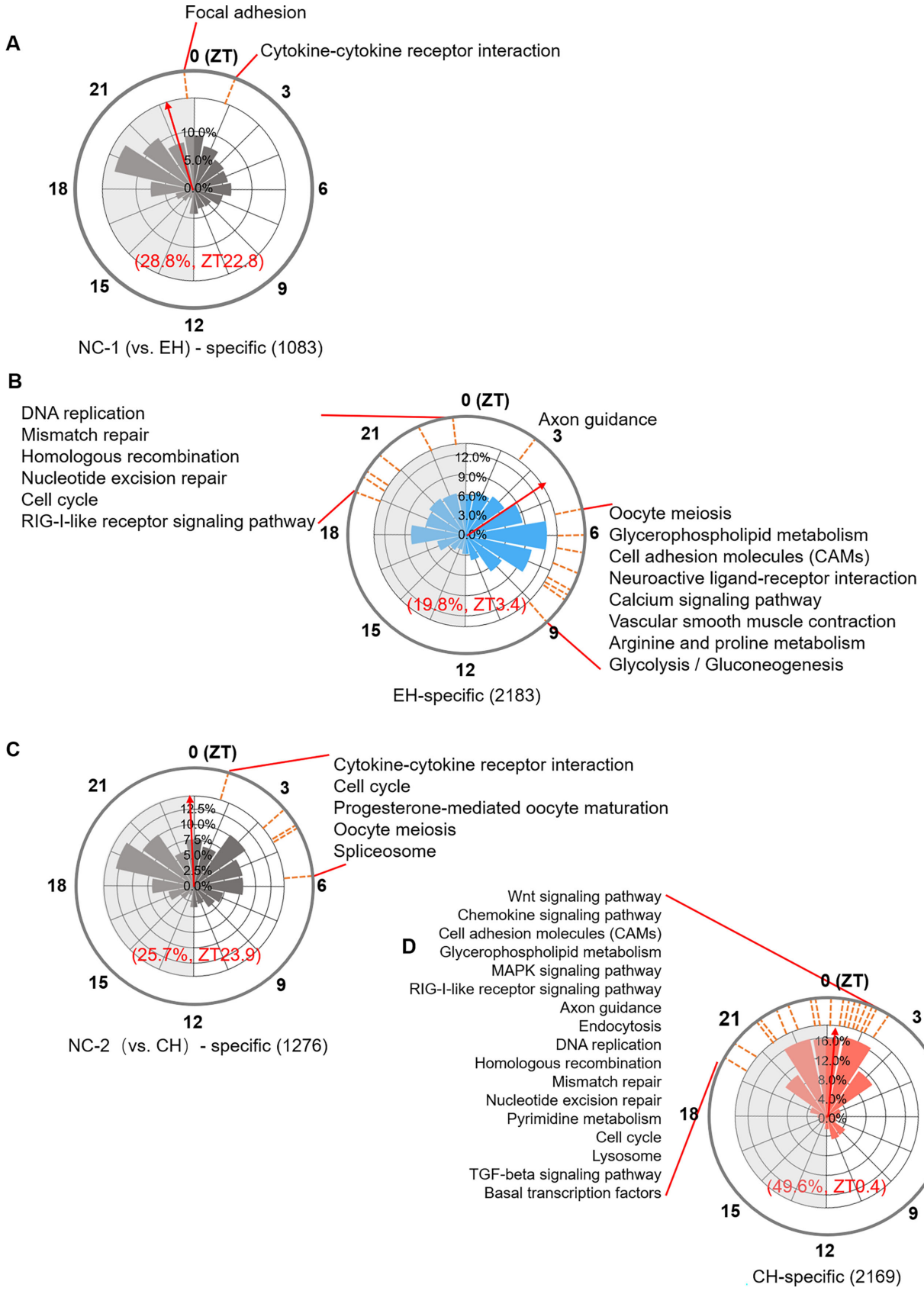

Figure 3. Temporal distribution of rhythmic gene functions under normoxia and hypoxia assessed by PSEA. (**A**–**D**) Rose plots illustrating the circadian phase distributions of significantly enriched KEGG pathways among rhythmic genes uniquely identified in NC (**A**, **C**), EH (**B**), and CH (**D**) groups. Each petal represents the proportion of genes within a KEGG pathway reaching peak expression during a 1.5-hour ZT interval. *Dashed lines* denote the phase timing of individual KEGG pathways, and *red arrows* indicate the mean phase vector direction. *Shaded areas* correspond to the dark phase (ZT12–ZT24).

Investigative Ophthalmology & Visual Science

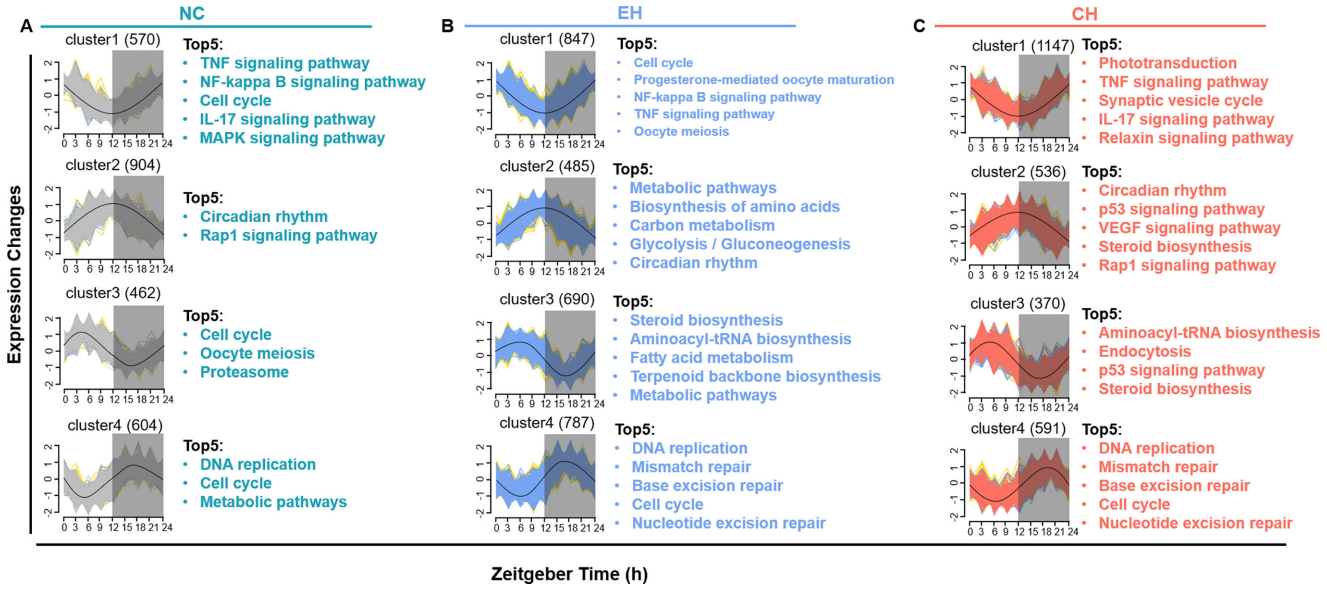

Figure 4. Time-series clustering of rhythmic gene expression in the mouse cornea under normoxia and hypoxia. (**A–C**) Rhythmic genes (P_adj < 0.01, identified by JTK_CYCLE) were clustered by temporal expression pattern using fuzzy C-means clustering under NC (**A**), EH (**B**), and CH (**C**) conditions. Each condition yielded four expression clusters. *Curves* represent standardized expression trajectories (Z-score) across eight circadian ZT points. *Shaded areas* indicate high-confidence cluster members (*gray* in NC, *blue* in EH, *red* in CH), and *yellow lines* denote low-confidence assignments. KEGG pathways significantly enriched (Q < 0.05) within each cluster are listed next to the corresponding plots.

showing a mean peak phase at ZT3.4 (Fig. 3B). In addition, EH-specific pathways displayed a bimodal phase distribution spanning both dark and early light phases.

Under CH, rhythmic gene enrichment was highly compressed and concentrated near the dark–light transition (ZT0.4), as indicated by sharp clustering in the rose plot (Fig. 3D). In contrast, NC-specific genes in an independent subset showed a more dispersed temporal distribution with a peak near ZT23.9 (Fig. 3C). These analyses indicate that both EH and CH alter the phase timing of rhythmic gene function in the cornea, with EH inducing a shift toward light-phase enrichment and CH exhibiting pronounced temporal consolidation around dawn.

Hypoxia Disrupts the Oscillatory Structure and Functional Dynamics of Circadian Gene Clusters in the Cornea

To characterize how hypoxia modulates temporal patterns of rhythmic gene expression, we performed fuzzy C-means clustering on JTK_CYCLE-identified rhythmic transcripts from NC, EH, and CH groups. Genes were grouped into four clusters per condition based on Z-score–normalized expression trajectories across eight ZT points (ZT0–ZT21), with each cluster representing a distinct phase of peak expression and associated biological functions (Figs. 4A–C).

In the NC group, Cluster 1 peaked near ZT0/24 and was enriched in pathways related to immune and inflammatory signaling, including tumor necrosis factor (TNF), nuclear factor kappa B (NF-κB), interleukin-17 (IL-17), and mitogen-activated protein kinase (MAPK) cascades. Cluster 2, peaking at ZT12, showed enrichment for Rap1 signaling and circadian rhythm genes. Cluster 3 peaked at ZT6 and contained genes involved in cell cycle regulation, meiosis, and proteasome activity. Cluster 4, with peak expression at ZT18, was associated with DNA replication, cell cycle progression, and metabolic pathways.

Under EH, Cluster 1 included genes peaking at ZT0/24 and was enriched for cell-cycle control, progesterone-mediated oocyte maturation, and TNF signaling. Cluster 2 (ZT12 peak) was associated with metabolic pathways, amino acid biosynthesis, carbon metabolism, and glycolysis/gluconeogenesis. Cluster 3 (ZT6 peak) showed enrichment in steroid biosynthesis, aminoacyl-transfer RNA (tRNA) biosynthesis, and fatty acid metabolism. Cluster 4 (ZT18 peak) was enriched in DNA repair–related pathways including mismatch repair and nucleotide excision repair.

In the CH group, Cluster 1 (ZT0/24) showed enrichment in phototransduction, TNF signaling, and synaptic vesicle cycling. Cluster 2 (ZT12) included pathways related to oxidative stress responses, such as p53 and vascular endothelial growth factor (VEGF) signaling. Cluster 3 (ZT6) was dominated by biosynthetic processes including aminoacyl-tRNA and steroid biosynthesis. Cluster 4 (ZT18) was comprised of genes involved in genome maintenance and repair, such as homologous recombination, base excision repair, and the cell cycle.

Together, these results show that both EH and CH reconfigure the temporal clustering of rhythmic genes in a phase-dependent and functionally distinct manner, with differences in pathway composition and peak timing under each condition.

Hypoxia Alters Core Clock-Gene Expression in a Phase-Dependent Manner

To evaluate the impact of hypoxia on the transcriptional dynamics of the corneal circadian clock, we examined 24-hour expression profiles of 12 core clock genes under NC,

Investigative Ophthalmology & Visual Science

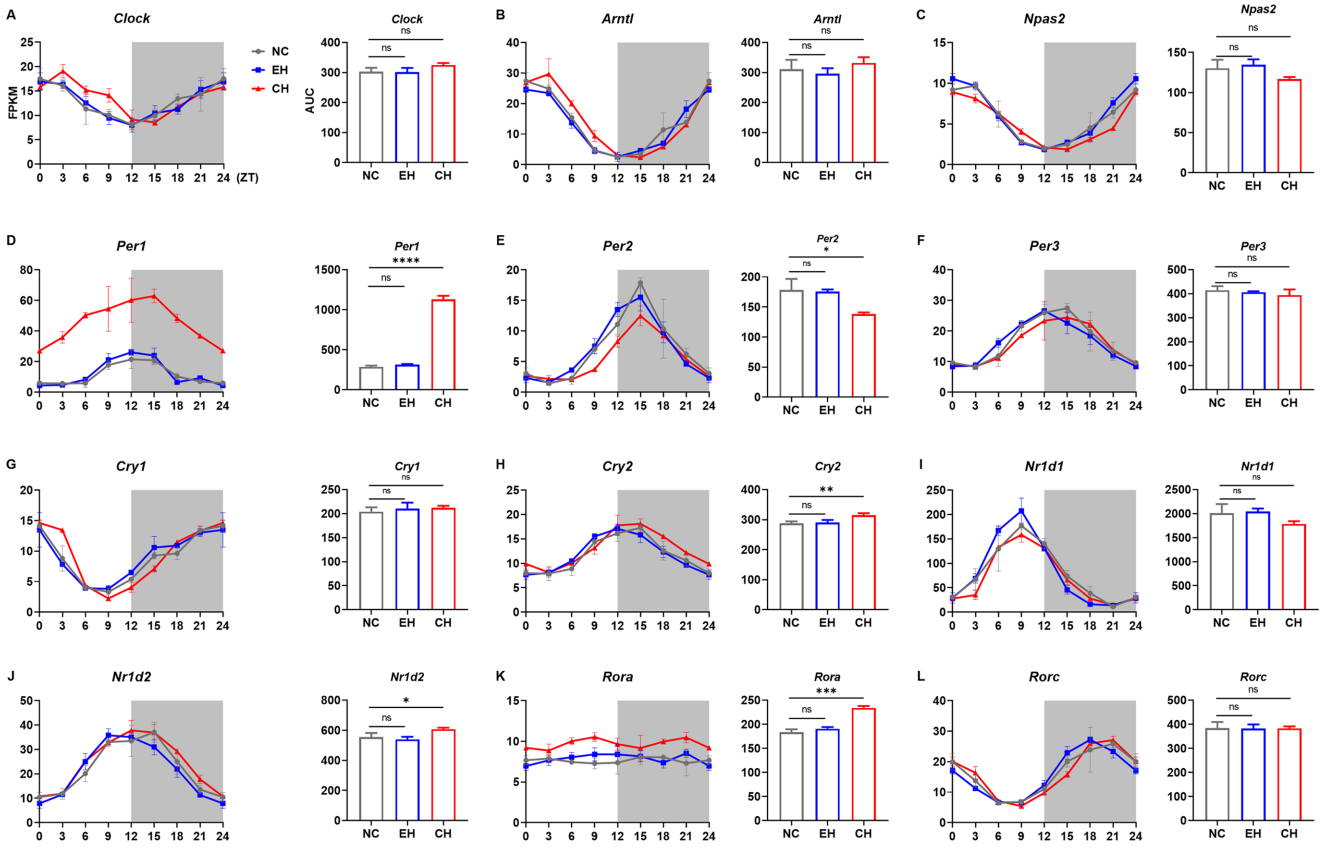

Figure 5. Temporal expression patterns of core circadian clock genes in the mouse cornea under normoxia and hypoxia. (**A–L**) ZT-dependent expression profiles of 12 core clock genes in the cornea across 24 hours under NC (*gray*), EH (*blue*), and CH (*red*) conditions. Each line plot displays mean transcript abundance ± SD at eight ZT points ($n = 3$). *Shaded areas* represent the dark phase (ZT12–ZT24). Adjacent bar graphs summarize the 24-hour AUC for each gene. Genes are grouped by functional classification: transcriptional activators (**A–C**), repressors (**D–H**), and nuclear receptors (**I–L**). $^{*}P < 0.05$, $^{**}P < 0.01$, $^{***}P < 0.001$, $^{****}P < 0.0001$; ns, no significance.

EH, and CH conditions. Gene expression was profiled at eight ZT points, and temporal oscillation patterns were compared across groups (Figs. 5A–L). Under NC conditions, all clock genes exhibited characteristic oscillatory expression with phase relationships consistent with a functional peripheral circadian loop. Genes in the transcriptional activator group (*Clock*, *Arntl*, *Npas2*) showed peak expression near ZT0 to ZT6 (Figs. 5A–C), and repressor genes (*Per1–Per3*, *Cry1*, *Cry2*) (Figs. 5D–H) and nuclear receptors (*Nr1d1*, *Nr1d2*, *Rora*, *Rorc*) (Figs. 5I–L) demonstrated expected antiphase behavior.

Exposure to EH had minimal effects on rhythmic gene architecture. Most genes retained their waveform shape, peak timing, and amplitude. Quantitative comparison of area under the curve (AUC) values revealed no significant differences between NC and EH groups, suggesting preserved circadian transcriptional output under short-term environmental oxygen reduction (Figs. 5A–L).

In contrast, CH altered the expression of several core clock components. Time-series profiles revealed increased expression of *Per1*, *Cry2*, *Nr1d2*, and *Rora* (Figs. 5D, 5H, 5J, 5K), whereas *Per2* (Fig. 5E) expression was reduced relative to NC and EH. These changes were reflected in elevated AUC values for the upregulated genes and diminished AUC for Per2. Altered amplitude and phase relationships were also observed in CH for multiple genes within the repressor and nuclear receptor arms of the clock. To further validate these findings, RT-qPCR was performed on all 12 core circadian clock genes. The results demonstrated that EH did not significantly affect the oscillatory patterns of core clock genes, whereas CH disrupted the rhythmicity of *Per1*, *Per2*, *Cry2*, *Nr1d2*, and *Rora*, consistent with the RNA-seq results (Supplementary Fig. S1).

These findings indicate that EH maintains overall clock gene rhythmicity, but CH induces gene-specific alterations in transcriptional amplitude and expression levels, particularly among nuclear receptors and negative feedback regulators of the circadian loop.

Hypoxia Induces Temporally Gated and Model-Specific Transcriptomic Remodeling in the Cornea

To assess the circadian-phase–specific dynamics of hypoxia-induced gene regulation, we performed differential expression and pathway enrichment analyses across eight ZT points in mouse corneas exposed to EH or CH. Time-resolved RNA-seq revealed marked temporal variation in transcriptomic responses, with the highest number of DEGs observed at ZT18 in both EH ($n = 821$) and CH ($n = 1126$), suggesting a shared peak of transcriptional sensitivity (Figs. 6A, 6B; Supplementary Table S3).

GSEA identified distinct regulatory programs enriched in each condition. In EH, upregulated genes were predominantly associated with immune pathways, including NF-κB,

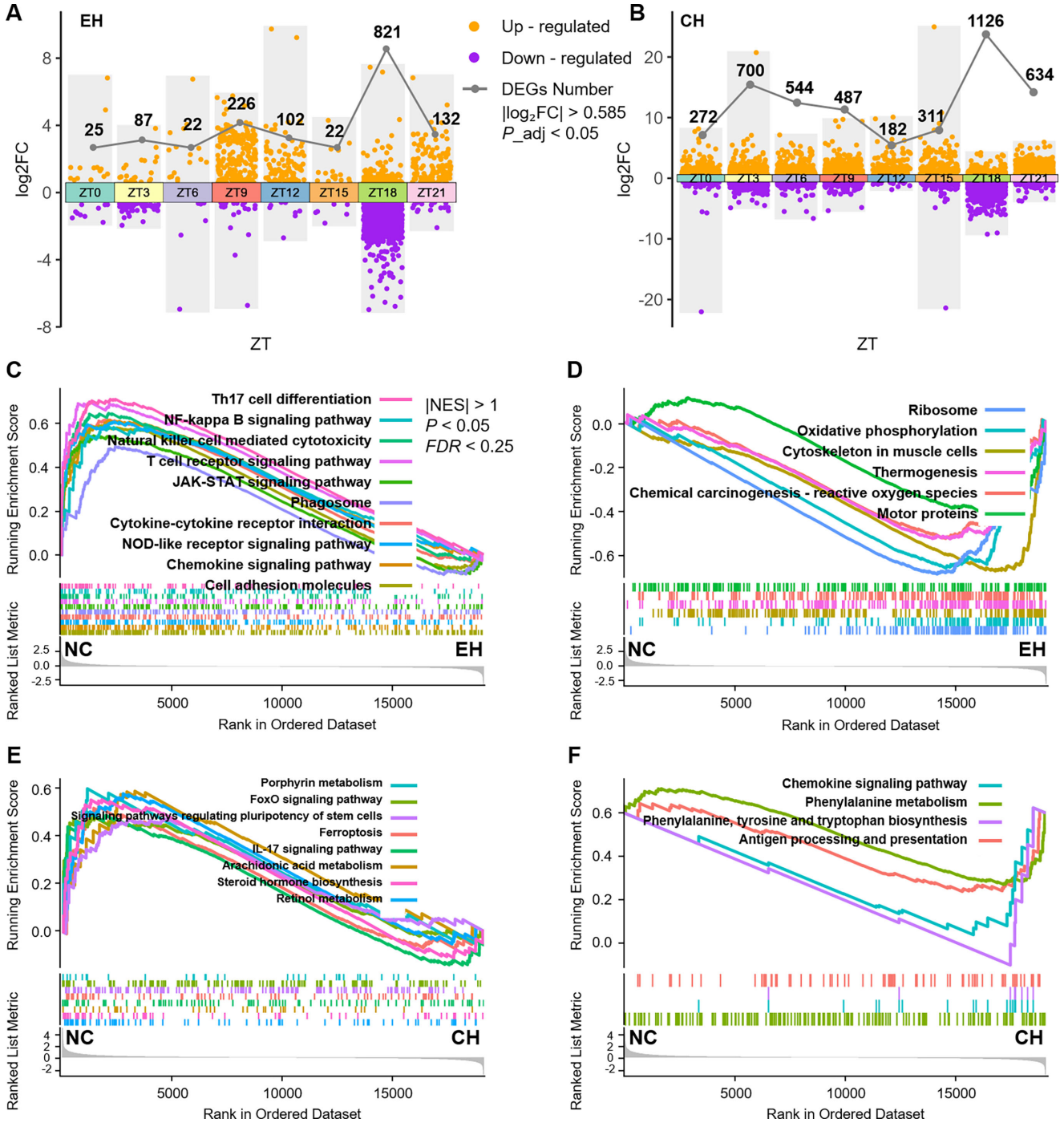

Figure 6. Global transcriptomic remodeling in the mouse cornea under EH and CH. (**A**, **B**) Differential expression analysis comparing NC with EH (**A**) and CH (**B**) across eight ZT points. Each data point represents the $\log_2$ FC at a given ZT. *Orange* and *purple dots* indicate significantly upregulated and downregulated genes, respectively (P_adj < 0.05, $|\log_2 \text{FC}| > 0.585$). Line plots show the total number of DEGs at each ZT. (**C**–**F**) GSEA of KEGG pathways enriched in EH (**C**, **D**) and CH (**E**, **F**) groups. Enrichment plots display the top 10 positively (**C**, **E**) and negatively (**D**, **F**) enriched pathways ranked by normalized enrichment score ($|\text{NES}| > 1$, $P < 0.05$, and FDR < 0.25). *Colored curves* correspond to individual pathways.

Janus kinase (JAK)/signal transducer and activator of transcription (STAT), and T-cell receptor pathways (Fig. 6C). Additional enrichment was noted in modules related to T-helper cell differentiation and cytokine–cytokine receptor interaction. In contrast, downregulated genes in EH were enriched in oxidative phosphorylation and ribosomal function (Fig. 6D).

CH exposure elicited broader transcriptomic alterations. Upregulated DEGs in this group were enriched for signaling modules such as FoxO and IL-17, as well as metabolic pathways including arachidonic acid metabolism and ferroptosis (Fig. 6E). Genesets related to stem cell pluripotency and retinoid metabolism were also represented. Downregulated genes were associated with immune surveillance and host

Investigative Ophthalmology & Visual Science

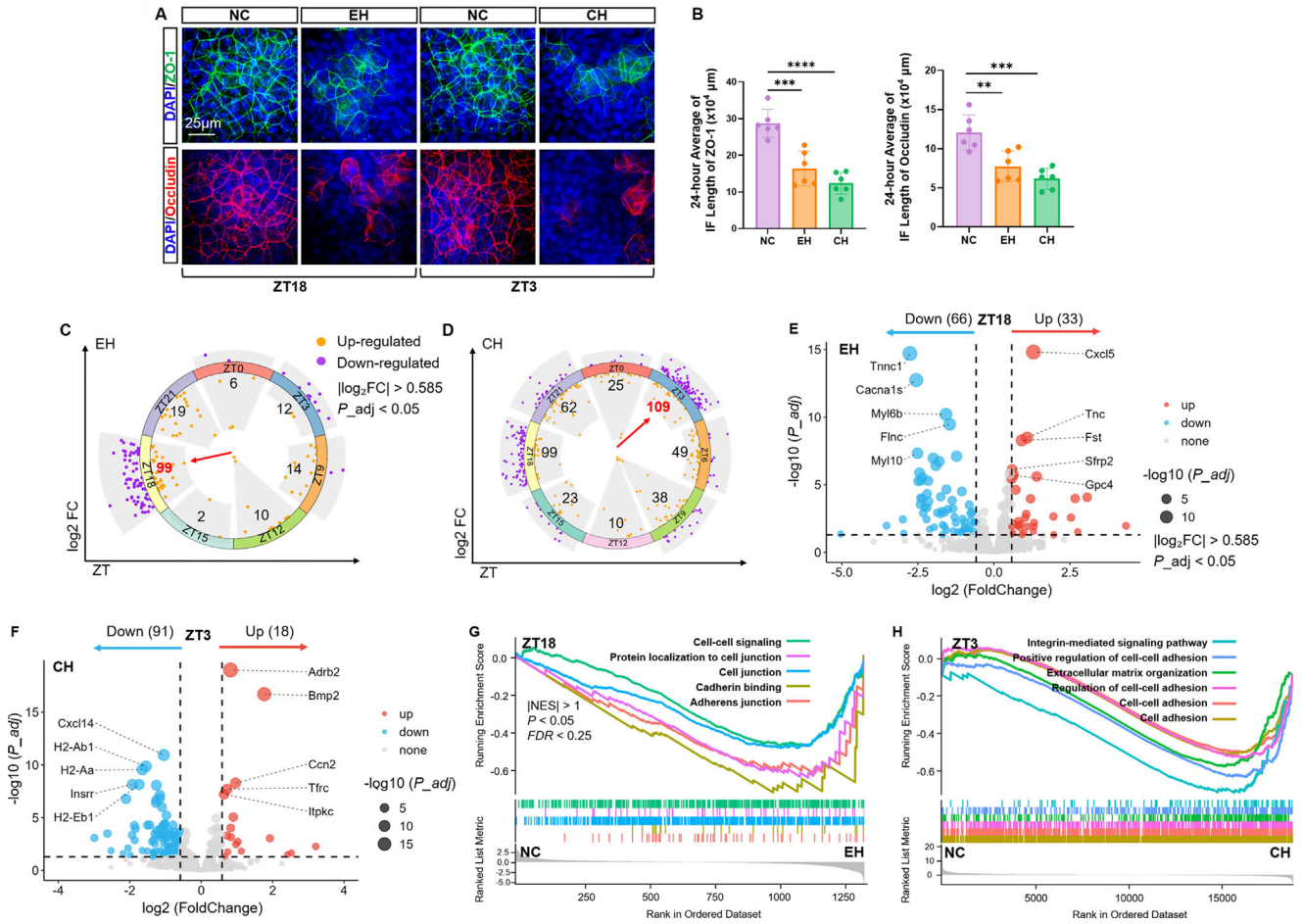

Figure 7. Circadian-phase–dependent disruption of corneal epithelial junctions under hypoxia. (**A**, **B**) Representative immunofluorescence images (**A**) and quantitative analysis (**B**) of tight junction protein ZO-1 (*green*) and occludin (*red*) in the corneal epithelium at ZT18 under NC and EH conditions and at ZT3 under NC and CH conditions. Nuclei were counterstained with DAPI (*blue*). *Scale bar*: 25 μm. $^{**}P < 0.01$, $^{***}P < 0.001$, $^{****}P < 0.0001$. (**C**, **D**) Circular volcano plots displaying the phase distribution of differentially expressed barrier-related genes (P_adj < 0.05, $|\log_2 \text{FC}| > 0.585$) in EH at ZT18 (**C**) and CH at ZT3 (**D**). *Orange dots* represent significantly upregulated genes; *purple dots* represent significantly downregulated genes. Numbers inside the inner circle indicate the number of DEGs, and *red arrows* indicate the circadian phase with the highest number of DEGs. (**E**, **F**) Volcano plots highlighting the top 10 most significantly altered genes at ZT18 under EH (**E**) and at ZT3 under CH (**F**). Upregulated and downregulated genes are depicted in *red* and *blue*, respectively. The size of each dot represents the $-\log_{10}$ (P_adj). (**G**, **H**) GSEA plots illustrating significantly altered barrier-related pathways at ZT18 under EH (**G**) and ZT3 under CH (**H**). Criteria for significance were set as normalized enrichment score $|\text{NES}| > 1$, $P < 0.05$, and FDR < 0.25.

defense processes, including antigen processing and amino acid metabolism (Fig. 6F).

These results indicate that both EH and CH induce temporally structured transcriptomic changes in the cornea, with ZT18 representing a shared phase of peak gene regulation. The distinct pathway enrichment patterns under EH and CH highlight divergent molecular responses to EH versus CH.

Hypoxia Modulates Corneal Barrier Function Through Circadian-Phase–Dependent Mechanisms

To evaluate the effects of hypoxia on epithelial junctional integrity, we examined the spatial distribution of ZO-1 and occludin in mouse corneas collected at ZT18/3 under NC, EH, and CH conditions (Fig. 7A). In NC corneas, both proteins exhibited continuous, polygonal membrane localization characteristic of intact tight junctions. By contrast, corneas from EH- and CH-exposed mice displayed discontinuous and fragmented staining patterns, indicative of junctional disorganization. Quantitative analysis of fluorescence signal continuity further confirmed a significant reduction in junctional integrity in both hypoxia models (Fig. 7B). In parallel, we continuously measured central corneal thickness (CCT) at ZT0, ZT8, ZT16, and ZT24 over a 24-hour cycle (Supplementary Figs. S2A, S2B) and assessed corneal permeability by fluorescein sodium staining (Supplementary Fig. S2C). Hypoxia exposure resulted in a marked increase in CCT, demonstrating that corneal structural parameters are highly sensitive to oxygen availability. In contrast, fluorescein staining scores remained unchanged, suggesting that this method is not sufficiently sensitive to detect early hypoxia-induced alterations in the cornea.

To determine whether these structural changes corresponded with transcriptional alterations, we analyzed the expression dynamics of 1352 junction-associated genes across the circadian cycle. Phase-distributed DEG analysis revealed temporal specificity in both models: 99 genes were differentially expressed at ZT18 in EH (Fig. 7C), and 109

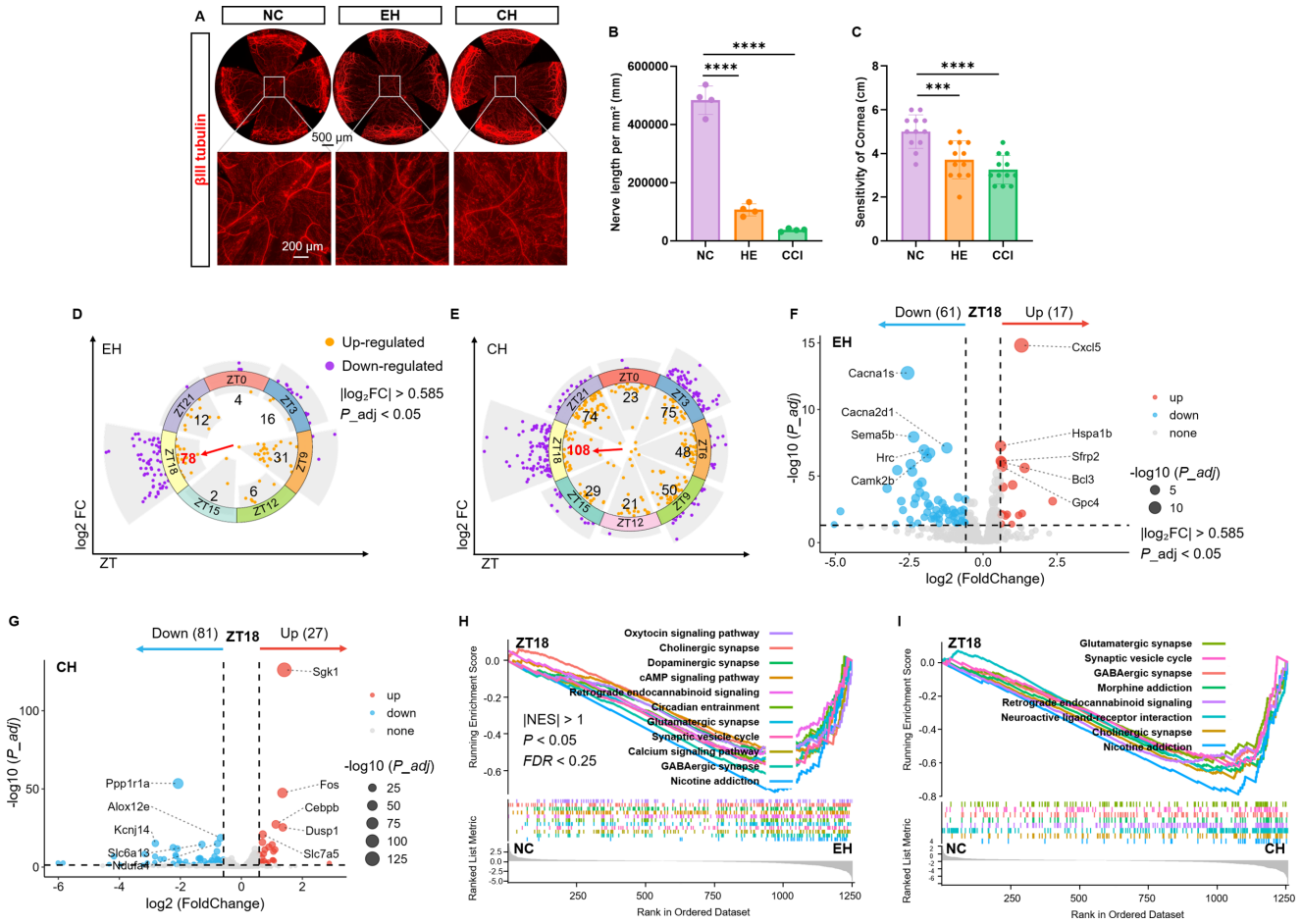

Figure 8. Neural remodeling and circadian-phase–dependent transcriptional alterations in the corneal subbasal nerve plexus under hypoxia. (**A**) Representative immunofluorescence images showing βIII-tubulin–labeled subbasal nerve plexus in mouse corneas under NC, EH, and CH conditions. *Scale bars*: 500 μm (main panels) and 200 μm (insets). (**B**) Quantitative analysis of subbasal nerve fiber density among the NC, EH, and CH groups ($n = 6$ per group). ****$P < 0.0001$. (**C**) Corneal mechanical sensitivity measured by blink reflex threshold using a Cochet–Bonnet esthesiometer ($n = 6$ per group). ***$P < 0.001$, ****$P < 0.0001$). (**D**, **E**) Circular volcano plots depicting the circadian phase distribution of DEGs (P_adj < 0.05, $|\log_2 FC| > 0.585$) associated with neural function in EH (**D**) and CH (**E**). *Orange dots* indicate significantly upregulated genes; *purple dots* represent significantly downregulated genes. *Numbers within inner circles* indicate total DEGs; *red arrows* denote the circadian phase with the highest number of DEGs. (**F**, **G**) Volcano plots highlighting the top 10 most significantly altered genes at ZT18 under EH (**F**) and CH (**G**). *Red* indicates upregulated genes, *blue* indicates downregulated genes, and *dot size* corresponds to the $-\log_{10}$ (P_adj). (**H**, **I**) GSEA plots showing significantly enriched neural signaling pathways at ZT18 under EH (**H**) and CH (**I**) conditions. Pathways shown met significance criteria: NES < -1, $P < 0.05$, and FDR < 0.25.

genes were altered at ZT3 in CH (Fig. 7D). In EH, upregulated genes included *Cxcl5*, *Tnc*, *Fst*, *Sfrp2*, and *Gpc4*, and downregulated genes such as *Tnnc1*, *Cacna1s*, *Myl6b*, *Flnc*, and *Myl10* were related to cytoskeletal and contractile elements (Fig. 7E). In CH, increased expression of *Adrb2*, *Bmp2*, *Ccn2*, *Tfrc*, and *Itpkc* coincided with reduced levels of *Cxcl14*, *H2-Ab1*, *H2-Aa*, *Insrr*, and *H2-Eb1* (Fig. 7F), indicating suppression of adhesion and immune-regulatory components. GSEA further revealed that junction-associated pathways were selectively downregulated at these critical time points. At ZT18 in EH, pathways such as adherens junction, cadherin binding, and cell–cell contact localization were reduced (Fig. 7G). At ZT3 in CH, ECM organization, integrin-mediated signaling, and cell adhesion pathways were diminished (Fig. 7H).

Together, these findings demonstrate that EH and CH impair epithelial junctional integrity through temporally distinct transcriptional mechanisms, with ZT18 and ZT3 representing respective windows of circadian vulnerability.

Hypoxia Modulates Corneal Neurofunction Through Circadian-Phase–Dependent Mechanisms

To evaluate the structural and functional impact of hypoxia on the corneal nervous system, we examined the subbasal nerve plexus using βIII-tubulin immunostaining in NC, EH, and CH groups (Fig. 8A). Compared with NC, both hypoxia models exhibited visibly reduced nerve fiber density (Fig. 8A), which was confirmed by quantitative image analysis (Fig. 8B). Consistent with this structural loss, corneal sensitivity, as measured by Cochet–Bonnet esthesiometry, was significantly reduced in hypoxia-exposed mice (Fig. 8C). Continuous assessment of corneal sensitivity at ZT0, ZT8, ZT16, and ZT24 over a 24-hour cycle yielded results consistent with these observations, further reinforcing the conclusion that hypoxia impairs corneal neural function (Supplementary Fig. S3).

To investigate whether neural gene expression was modulated in a circadian-phase–dependent manner, we

Investigative Ophthalmology & Visual Science

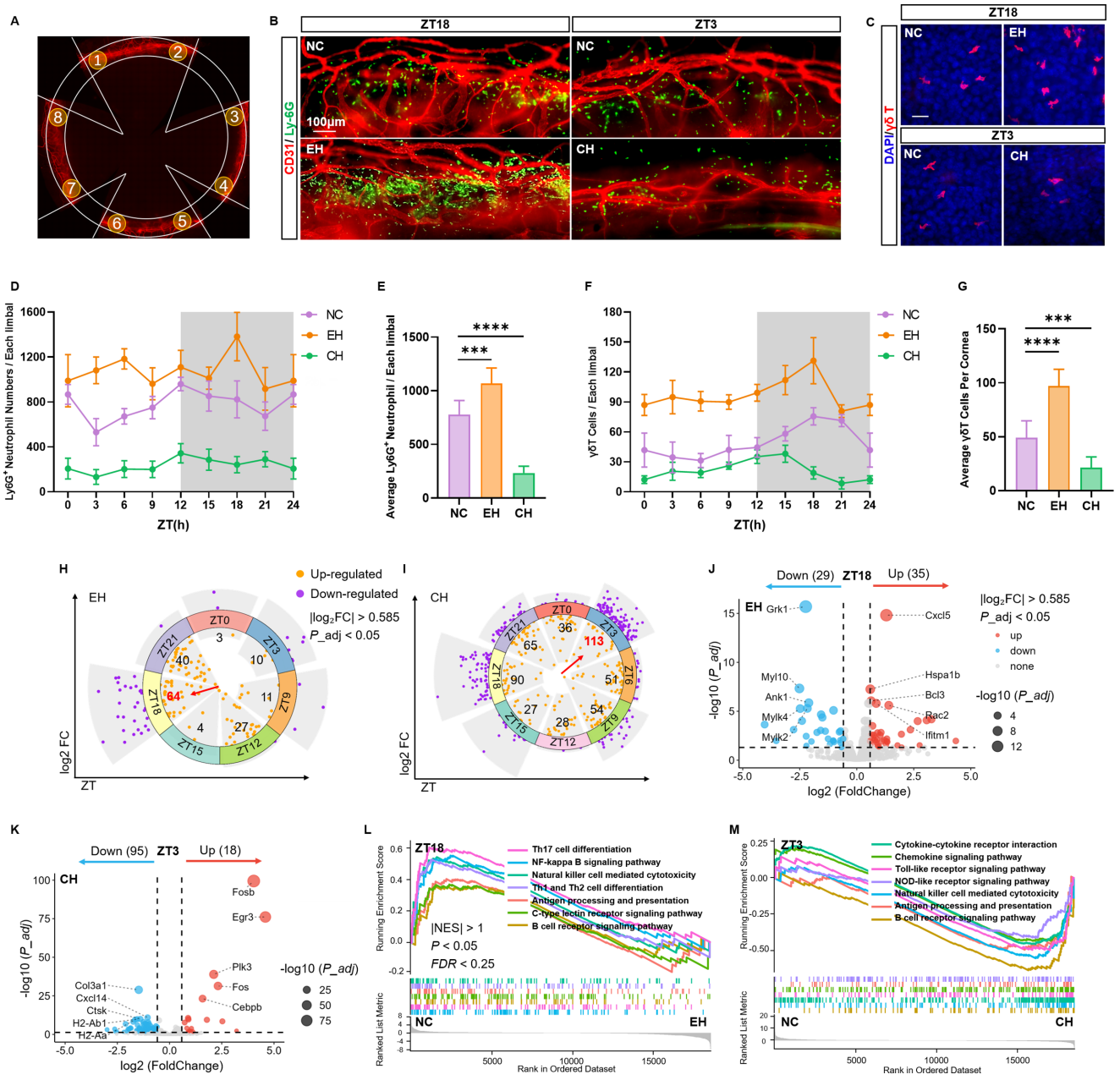

Figure 9. Circadian-phase–specific modulation of corneal immune activity under EH and CH. (**A**) Schematic diagram illustrating the region of interest (limbal area) used for counting neutrophils and $\gamma\delta$ T cells in mouse corneas. The cells across eight fields (from field 1 to 8, under 40× microscopic view) were counted. (**B**) Representative immunofluorescence images of Ly6G$^+$ neutrophils (*green*) and blood vessels (*red*) in the corneal limbal region under NC and EH conditions at ZT18, and under NC and CH conditions at ZT3. *Scale bar*: 100 μm. (**C**) Representative immunofluorescence images of $\gamma\delta$ T cells (*red*) in the corneal limbus at ZT18 under NC and EH conditions and at ZT3 under NC and CH conditions. Nuclei were counterstained with DAPI (*blue*). *Scale bar*: 25 μm. (**D–G**) Temporal profiles showing neutrophil (**D**) and $\gamma\delta$ T cell (**F**) counts across ZT points in NC, EH, and CH groups. Mean numbers of neutrophils (**E**) and $\gamma\delta$ T cells (**G**) averaged over the entire circadian cycle in each group ($n = 6$ per group). ***$P < 0.001$, ****$P < 0.0001$. (**H**, **I**) Circular volcano plots depicting the circadian-phase distribution of immune-related DEGs (P_adj < 0.05, $|\log_2 FC| > 0.585$) under EH (**H**) and CH (**I**) conditions. *Orange dots* represent significantly upregulated genes; *purple dots* represent significantly downregulated genes. *Numbers within inner circles* indicate the total number of DEGs, and *red arrows* denote the circadian phase with the highest DEG counts. (**J**, **K**) Volcano plots highlighting the top 10 most significantly altered immune-related genes at ZT18 under EH (**J**) and ZT3 under CH (**K**) conditions. Upregulated genes are indicated in *red*, downregulated genes in *blue*. *Dot size* corresponds to $-\log_{10}$ (P_adj). (**L**, **M**) GSEA plots illustrating significantly altered immune signaling pathways at ZT18 under EH conditions (NES > 1, $P < 0.05$, FDR < 0.25) (**L**) and at ZT3 under CH conditions (NES < -1, $P < 0.05$, FDR < 0.25) (**M**).

analyzed 1275 transcripts associated with neurotransmission and synaptic signaling across the circadian cycle. Both EH and CH induced peak differential gene expression at ZT18, with 78 DEGs detected in EH and 108 in CH (Figs. 8D, 8E). In EH, upregulated genes at ZT18 included *Cxcl5*, *Hspa1b*, *Sfrp2*, *Bcl3*, and *Gpc4*, and downregulated genes such as *Cacna1s*, *Cacna2d1*, *Sema5b*, *Hrc*, and *Camk2b* were involved in calcium signaling and synaptic transmission (Fig. 8F). In CH, upregulated genes included *Sgk1*, *Fos*, *Cebpb*, *Dusp1*, and *Slc7a5*, whereas genes linked to mitochondrial and ion transport functions, such as *Ppp1r1a*, *Alox12e*, *Kcnj14*, *Slc6a13*, and *Ndufa4* were downregulated (Fig. 8G).

GSEA revealed broad downregulation of neural signaling pathways at ZT18 under both hypoxia models. In EH, repressed KEGG pathways included GABAergic synapse, glutamatergic synapse, synaptic vesicle cycle, circadian entrainment, and calcium signaling (Fig. 8H). In CH, additional suppression was observed in neuroactive ligand–receptor interaction, dopaminergic signaling, and addiction-related pathways (Fig. 8I). These results indicate that both EH and CH compromise corneal neurofunction through transcriptional repression of key neurotransmission pathways in a circadian-phase–specific manner, with ZT18 emerging as a common time point of maximal impairment.

Hypoxia Modulates Corneal Immune Activity Through Circadian-Phase–Dependent Mechanisms

To investigate the impact of hypoxia on corneal immune regulation, we performed time-resolved immunostaining of immune cell populations in the limbal region under NC, EH, and CH conditions (Fig. 9A). In EH-treated corneas, both Ly6G$^+$ neutrophils and $\gamma\delta$ T cells were increased across the circadian cycle compared to NC (Figs. 9B–G). In contrast, CH-exposed corneas exhibited a marked reduction in both immune cell types, suggesting suppressed immune presence (Figs. 9B–G).

To characterize underlying transcriptional changes, we analyzed the temporal distribution of immune-related DEGs. In EH, peak transcriptional alterations were observed at ZT18, including 64 DEGs (35 upregulated, 29 downregulated) (Fig. 9H). Upregulated genes included *Cxcl5*, *Hspa1b*, *Bcl3*, *Rac2*, and *Ifitm1*, and downregulated genes such as *Grk1*, *Myl10*, *Ank1*, *Mylk4*, and *Mylk2* were associated with cytoskeletal structure and signaling (Fig. 9J). In CH, the largest immune-related transcriptional shift occurred at ZT3, with 113 DEGs identified (Fig. 9I). This included upregulation of *Fosb*, *Egr3*, *Plk3*, *Fos*, and *Cebpb*, alongside reduced expression of immune surveillance genes including *Col3a1*, *Cxcl14*, *Ctsk*, *H2-Ab1*, and *H2-Aa* (Fig. 9K).

GSEA revealed divergent pathway-level regulation between conditions. At ZT18, EH corneas showed enrichment of immune activation pathways such as B-cell receptor signaling, NF-κB signaling, and Th17 differentiation (Fig. 9L). In contrast, CH corneas at ZT3 showed widespread suppression of immune response pathways, including cytokine–cytokine receptor interaction, Toll-like receptor signaling, and complement cascades (Fig. 9M).

These results demonstrate that hypoxia alters corneal immune dynamics in a circadian-phase–dependent manner, with immune activation occurring at ZT18 under EH and immune suppression prevailing at ZT3 under CH.

Discussion

Using time-series transcriptomics plus barrier, neural, and immune assays, we demonstrated that EH and CH each rewire approximately 30% of the corneal rhythmic transcriptome in a model- and phase-dependent fashion. These changes coincide with loss of epithelial integrity, nerve density, and immune balance, revealing phases when the corneal clock is least able to mitigate hypoxic stress. Peak disruption converges at ZT18 and, secondarily, ZT3, revealing circadian phases of heightened vulnerability during which the peripheral corneal clock is least able to buffer oxygen stress (Fig. 10). Below, we integrate these findings with current literature, emphasize their translational relevance, and outline future directions.

Hypoxia Reshapes Circadian Phase Architecture Via Model-Specific Mechanisms

Chemical hypoxia ($CoCl_2$) stabilizes *HIF-1α*, which docks at hypoxia-response elements flanking E-box motifs and transcriptionally activates *Per1*, *Cry2*, *Nr1d2*, and *Rora*.[36,37] EH, by contrast, preferentially engages *BMAL1*-driven programs that upregulate mitochondrial dynamics and oxidative phosphorylation genes as documented in liver and brain.[38,39] The modest (<20%) overlap between EH- and CH-responsive rhythmic genes therefore reflects two partially independent conduits: (1) HIF-centered transcriptional rewiring and (2) *BMAL1*-dependent metabolic reprogramming that recruits the nicotinamide adenine dinucleotide (NAD^+)/sirtuin 1 (SIRT1) axis, reactive oxygen species (ROS) buffering, and AMP-activated protein kinase (AMPK) signaling.[40] Such bifurcation reconciles the shared phenotypes yet divergent signatures of the two models. EH further preserves retinal or suprachiasmatic nucleus (SCN) Zeitgeber cues, whereas systemically delivered CH overrides local O_2 sensing and adds a layer of cobalt-induced oxidative stress via Fenton chemistry.

Circadian Phase Dictates Functional Outcomes of Hypoxic Disruption

ZT18 emerges as a shared nadir, characterized by downregulation of junctional proteins (ZO-1, claudins, occludin), reduced βIII-tubulin, and a surge of neutrophil influx.[41] This coincides with the nighttime decline in adenosine triphosphate and antioxidant reserves,[42] suggesting that metabolic insufficiency underlies barrier fragility. The phenomenon echoes hepatic and myocardial studies in which hypoxia or ischemia–reperfusion elicits time-of-day–specific differences in infarct size and autophagy.[43,44] CH alone produces a second dip at ZT3, distinguished by suppressed chemokine and complement transcripts and blunted $\gamma\delta$ T-cell recruitment, implicating REV-ERBα/β–mediated immune quiescence.[45,46] Such dual-phase vulnerability reconciles reports that corneal hypoxia appears tolerable in daylight assays yet proves deleterious at night. In obstructive sleep apnea patients, analogous nocturnal O_2 dips elevate *PER1/HIF-1α* expression and tear cytokines, underscoring the clinical relevance of our murine findings.[6,47]

Circadian Control of Neural and Immune Programs Is Disrupted by Sustained Hypoxia

Both EH and CH downshift GABAergic, glutamatergic, and calcium-channel modules at ZT18,[48] pointing to

Investigative Ophthalmology & Visual Science

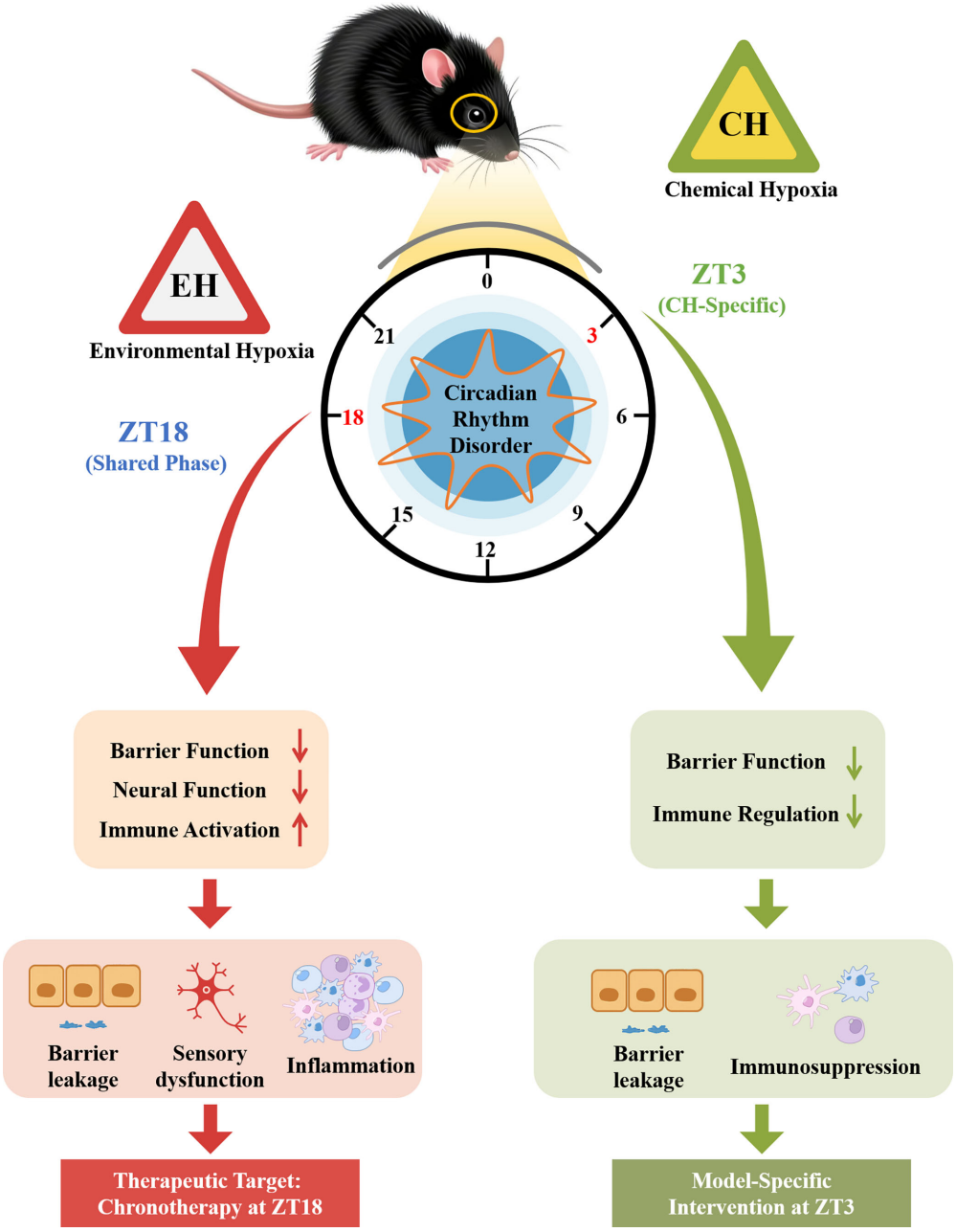

Figure 10. Hypoxia-induced circadian disruption triggers phase-dependent structural and immune dysfunction in the cornea. This schematic illustrates the circadian-phase–specific impact of EH and CH on corneal homeostasis. Both models converge at ZT18, a shared vulnerability phase, characterized by compromised epithelial barrier function (reduced ZO-1 and occludin expression), impaired neural activity (decreased βIII-tubulin expression and corneal sensitivity), and increased immune cell infiltration (Ly6G$^+$ neutrophils and $\gamma\delta$ T cells increase), collectively contributing to barrier leakage, sensory dysfunction, and inflammatory activation. In contrast, CH exhibits a model-specific immunosuppressive profile at ZT3, including downregulation of barrier markers and a decrease in the number of Ly6G$^+$ neutrophils and $\gamma\delta$ T cells, indicative of attenuated immune activity. The figure highlights ZT18 as a potential therapeutic window for chronotherapy and ZT3 as a CH-specific regulatory phase for targeted intervention.

compromised synaptic vesicle release and axon maintenance. Loss of calcitonin gene-related peptide (CGRP)- and acetylcholine-mediated restraint on resident macrophages permits increased *CX3CR1*$^+$ macrophage and Ly6G$^+$ neutrophil infiltration,[49,50] promoting a positive-feedback inflammatory response. In obstructive sleep apnea patients, analogous nocturnal O_2 dips elevate *PER1/HIF-1α* and tear cytokines, underscoring translational relevance.[6,7] Future single-cell and spatial-omics will be essential to map how hypoxia reshapes the neuroimmune lattice across stromal, epithelial, and endothelial niches.

Translational and Therapeutic Implications

Identification of ZT18 as a universal fault line thus supports clock-guided interventions. Ultra-permeable silicone hydrogel lenses deployed before sleep,[51] short-acting HIF inhibitors,[52] NAD$^+$ boosters,[53] or α_1-adrenergic antag-

Investigative Ophthalmology & Visual Science

onists[54] scheduled to precede ZT18 could blunt nighttime barrier loss and neuroimmune dysregulation. Chronotherapeutic design should incorporate wearable actigraphy,[55] salivary dim-light melatonin onset,[56] or tear-fluid *PER1* oscillation[57] as phase biomarkers and adopt adaptive dosing algorithms already piloted in oncology.

Experimental Models Reflect Distinct Hypoxic Etiologies

EH mimics intermittent external hypoxia such as that produced by eyelid closure[58] or high-altitude exposure,[59] whereas CH recreates sustained intracellular hypoxia by chemically stabilizing *HIF-1α* with cobalt chloride.[60] The complementary fingerprints of these models endorse a "two-hit" paradigm in which intermittent EH superimposed on sustained CH mirrors multifactorial clinical scenarios—for example, overnight contact-lens wear complicated by systemic hypoxemia.[61] Incorporating chromatin immunoprecipitation (ChIP) sequencing for *CLOCK*, *BMAL1*, and *HIF-1α* in corneas subjected to combined EH/CH will determine whether shared *cis*-elements (E-box, HRE, RORE) regulate the observed transcriptome realignment.

Study Limitations and Future Directions

This study identified ZT18 and ZT3 as potential phases of vulnerability to hypoxia-induced ocular surface injury, yet direct evidence of phase-specific treatment efficacy remains lacking. Similar to time-dependent therapeutic strategies in cardiac and neural hypoxia,[62–65] future work should implement circadian-phase–targeted interventions (e.g., pharmacological agents or oxygen-enhancing approaches) and assess corneal sensitivity, thickness, and permeability to validate therapeutic timing.

Several additional factors warrant consideration. Psychological stress suppresses tear secretion via the noradrenaline (NA)–α1a-adrenergic receptor (Adra1a)–Ucp2 pathway,[54] but its interaction with hypoxia—particularly at ZT18—remains unexplored. Biological variables also shape clock–hypoxia interactions: Estrogen stabilizes HIF-1α,[40,66] and aging attenuates BMAL1 amplitude in ocular tissues,[67] highlighting the need for lifespan- and sex-stratified models that better reflect clinical scenarios such as nightly contact lens wear or obstructive sleep apnea.[7] Moreover, behavioral readouts (blink dynamics, tear flow, visual acuity) were not captured; incorporating high-speed video-oculography and tear-osmolarity telemetry could bridge molecular and functional outcomes.[68] Finally, time-matched trials of α_1-adrenergic antagonists, NAD^+ boosters, HIF modulators, or highly oxygen-permeable lenses—administered just before the ZT18 nadir—will be crucial to test whether clock-centered therapies can interrupt stress–hypoxia feedback and enhance ocular surface function.

Conclusions

The circadian clock is a key determinant of corneal resilience to hypoxia. This study identifies ZT18 as a universal phase of heightened vulnerability and ZT3 as a model-specific window, marked by transcriptomic misalignment, epithelial barrier disruption, and neuroimmune imbalance. These findings highlight the potential of circadian-phase–based interventions to mitigate hypoxia-related ocular surface injury. Although we have not yet demonstrated direct differences in treatment efficacy across phases, future studies should test phase-targeted interventions—such as pharmacological agents or highly oxygen-permeable contact lenses—and evaluate outcomes including corneal sensitivity, thickness, and permeability. Such work will be critical to validate whether clock-informed strategies can optimize therapy and to support the incorporation of circadian phase into clinical trial design for ocular surface disease.

Acknowledgments

Supported by grants from the National Natural Science Foundation of China (Nos. 82101089, 82171014, and 81770962 to ZL) and the Basic Science Project of Henan Eye Institute/Henan Eye Hospital (No. 21JCZD001 to ZL).

Disclosure: **J. Liu**, None; **Y. Jing**, None; **J. Wu**, None; **D. Lu**, None; **Z. Li**, None

References

1. Raut AK, Mohapatra S, Siddiqu IG, et al. The human cornea: unraveling its structural, chemical, and biochemical complexities. *Chem Biodivers*. 2025;22:e202402224.
2. Forrester JV, McMenamin PG. Evolution of the ocular immune system. *Eye (Lond)*. 2025;39:468–477.
3. Zhu J, Yang L, Yang Q, et al. Kirigami-inspired breathable smart contact lens for wireless monitoring of corneal hypoxia and microenvironment. *Adv Healthc Mater*. 2025;14:e2402148.
4. Aguilella-Arzo M, Compañ V. A three-dimensional model to describe complete human corneal oxygenation during contact lens wear. *J Biomed Mater Res B Appl Biomater*. 2023;111:610–621.
5. Wang Y, Yu X, Liu Z, et al. Influence of hypobaric hypoxic conditions on ocular structure and biological function at high altitudes: a narrative review. *Front Neurosci*. 2023;17:1149664.
6. Wang S, He X, Li Q, et al. Obstructive sleep apnea affects lacrimal gland function. *Invest Ophthalmol Vis Sci*. 2022;63:3.
7. Koritala BSC, Lee YY, Gaspar LS, et al. Obstructive sleep apnea in a mouse model is associated with tissue-specific transcriptomic changes in circadian rhythmicity and mean 24-hour gene expression. *PLoS Biol*. 2023;21:e3002139.
8. Peek CB, Levine DC, Cedernaes J, et al. Circadian clock interaction with HIF1α mediates oxygenic metabolism and anaerobic glycolysis in skeletal muscle. *Cell Metab*. 2017;25:86–92.
9. Xue Y, Liu P, Wang H, et al. Modulation of circadian rhythms affects corneal epithelium renewal and repair in mice. *Invest Ophthalmol Vis Sci*. 2017;58:1865–1874.
10. Takahashi JS. Transcriptional architecture of the mammalian circadian clock. *Nat Rev Genet*. 2017;18:164–179.
11. Peek CB. Metabolic implications of circadian-HIF crosstalk. *Trends Endocrinol Metab*. 2020;31:459–468.
12. Liu S, Liu J, Xiang J, et al. Restorative effects of short-chain fatty acids on corneal homeostasis disrupted by antibiotic-induced gut dysbiosis. *Am J Pathol*. 2025;195:770–796.
13. Hughes ME, Hogenesch JB, Kornacker K. JTK_CYCLE: an efficient nonparametric algorithm for detecting rhythmic components in genome-scale data sets. *J Biol Rhythms*. 2010;25:372–380.
14. Subramanian A, Tamayo P, Mootha VK, et al. Gene set enrichment analysis: a knowledge-based approach for inter-

preting genome-wide expression profiles. *Proc Natl Acad Sci USA*. 2005;102:15545–15550.
15. Zhang R, Podtelezhnikov AA, Hogenesch JB, Anafi RC. Discovering biology in periodic data through phase set enrichment analysis (PSEA). *J Biol Rhythms*. 2016;31:244–257.
16. Kumar L, Futschik ME. Mfuzz: a software package for soft clustering of microarray data. *Bioinformation*. 2007;2:5–7.
17. Futschik ME, Carlisle B. Noise-robust soft clustering of gene expression time-course data. *J Bioinform Comput Biol*. 2005;3:965–988.
18. Ikenouchi J, Umeda K, Tsukita S, Furuse M, Tsukita S. Requirement of ZO-1 for the formation of belt-like adherens junctions during epithelial cell polarization. *J Cell Biol*. 2007;176:779–786.
19. Ljubimov AV, Saghizadeh M. Progress in corneal wound healing. *Prog Retin Eye Res*. 2015;49:17–45.
20. Li Z, Burns AR, Smith CW. Two waves of neutrophil emigration in response to corneal epithelial abrasion: distinct adhesion molecule requirements. *Invest Ophthalmol Vis Sci*. 2006;47:1947–1955.
21. Wang H, Xiao C, Dong D, et al. Epothilone B speeds corneal nerve regrowth and functional recovery through microtubule stabilization and increased nerve beading. *Sci Rep*. 2018;8:2647.
22. Carissimo G, Xu W, Kwok I, et al. Whole blood immunophenotyping uncovers immature neutrophil-to-VD2 T-cell ratio as an early marker for severe COVID-19. *Nat Commun*. 2020;11:5243.
23. Xue Y, Xu P, Hu Y, et al. Stress systems exacerbate the inflammatory response after corneal abrasion in sleep-deprived mice via the IL-17 signaling pathway. *Mucosal Immunol*. 2024;17:323–345.
24. Yuan X, Qi H, Li X, et al. Disruption of spatiotemporal hypoxic signaling causes congenital heart disease in mice. *J Clin Invest*. 2017;127:2235–2248.
25. Dachs GU, Patterson AV, Firth JD, et al. Targeting gene expression to hypoxic tumor cells. *Nat Med*. 1997;3:515–520.
26. Chen X, Li Y, Lu L, et al. Activation of the SST-SSTR5 signaling pathway enhances corneal wound healing in diabetic mice. *Mucosal Immunol*. 2024;17:858–870.
27. Liu J, Huang S, Yu R, et al. TRPV1^{+} sensory nerves modulate corneal inflammation after epithelial abrasion via RAMP1 and SSTR5 signaling. *Mucosal Immunol*. 2022;15:867–881.
28. Li Z, Burns AR, Han L, Rumbaut RE, Smith CW. IL-17 and VEGF are necessary for efficient corneal nerve regeneration. *Am J Pathol*. 2011;178:1106–1116.
29. Chucair-Elliott AJ, Zheng M, Carr DJ. Degeneration and regeneration of corneal nerves in response to HSV-1 infection. *Invest Ophthalmol Vis Sci*. 2015;56:1097–1107.
30. Huang Y, Fu T, Jiao X, et al. Hypothyroidism affects corneal homeostasis and wound healing in mice. *Exp Eye Res*. 2022;220:109111.
31. Zou S, Jiao X, Liu J, et al. High-fat nutritional challenge reshapes circadian signatures in murine extraorbital lacrimal glands. *Invest Ophthalmol Vis Sci*. 2022;63:23.
32. Huang S, Si H, Liu J, et al. Sleep loss causes dysfunction in murine extraorbital lacrimal glands. *Invest Ophthalmol Vis Sci*. 2022;63:19.
33. Jiao X, Pei X, Lu D, et al. Microbial reconstitution improves aging-driven lacrimal gland circadian dysfunction. *Am J Pathol*. 2021;191:2091–2116.
34. Jiao X, Wu M, Lu D, Gu J, Li Z. Transcriptional profiling of daily patterns of mRNA expression in the C57BL/6J mouse cornea. *Curr Eye Res*. 2019;44:1054–1066.
35. Lu D, Lin C, Jiao X, et al. Short-term high fructose intake reprograms the transcriptional clock rhythm of the murine extraorbital lacrimal gland. *Invest Ophthalmol Vis Sci*. 2019;60:2038–2048.
36. Wu Y, Tang D, Liu N, et al. Reciprocal regulation between the circadian clock and hypoxia signaling at the genome level in mammals. *Cell Metab*. 2017;25:73–85.
37. O'Connell EJ, Martinez CA, Liang YG, Cistulli PA, Cook KM. Out of breath, out of time: interactions between HIF and circadian rhythms. *Am J Physiol Cell Physiol*. 2020;319:C533–C540.
38. Jacobi D, Liu S, Burkewitz K, et al. Hepatic Bmal1 regulates rhythmic mitochondrial dynamics and promotes metabolic fitness. *Cell Metab*. 2015;22:709–720.
39. Dandavate V, Bolshette N, Van Drunen R, et al. Hepatic BMAL1 and HIF1α regulate a time-dependent hypoxic response and prevent hepatopulmonary-like syndrome. *Cell Metab*. 2024;36:2038–2053.e5.
40. Chang HC, Guarente L. SIRT1 mediates central circadian control in the SCN by a mechanism that decays with aging. *Cell*. 2013;153:1448–1460.
41. Wang Y, Wang Q, Dou S, Zhou Q, Xie L. Sleep deprivation induces corneal endothelial dysfunction by downregulating Bmal1. *BMC Ophthalmol*. 2024;24:268.
42. Richardson RB, Mailloux RJ. Mitochondria need their sleep: redox, bioenergetics, and temperature regulation of circadian rhythms and the role of cysteine-mediated redox signaling, uncoupling proteins, and substrate cycles. *Antioxidants (Basel)*. 2023;12:674.
43. Durgan DJ, Pulinilkunnil T, Villegas-Montoya C, et al. Short communication: ischemia/reperfusion tolerance is time-of-day-dependent: mediation by the cardiomyocyte circadian clock. *Circ Res*. 2010;106:546–550.
44. Wang H, Guo M, Ren B, et al. Circadian control of hepatic ischemia/reperfusion injury via HSD17B13-mediated autophagy in hepatocytes. *J Hepatol*. 2025;83:750–767.
45. Griffin P, Dimitry JM, Sheehan PW, et al. Circadian clock protein Rev-erbα regulates neuroinflammation. *Proc Natl Acad Sci USA*. 2019;116:5102–5107.
46. Shivshankar P, Fekry B, Eckel-Mahan K, Wetsel RA. Circadian clock and complement immune system-complementary control of physiology and pathology? *Front Cell Infect Microbiol*. 2020;10:418.
47. Gabryelska A, Turkiewicz S, Gajewski A, et al. Elucidating the interplay of hypoxia-inducible factor and circadian clock signaling in obstructive sleep apnea patients. *Int J Mol Sci*. 2025;26:971.
48. Crosson LA, Kroes RA, Moskal JR, Linsenmeier RA. Gene expression patterns in hypoxic and post-hypoxic adult rat retina with special reference to the NMDA receptor and its interactome. *Mol Vis*. 2009;15:296–311.
49. Yuan K, Zheng J, Shen X, et al. Sensory nerves promote corneal inflammation resolution via CGRP mediated transformation of macrophages to the M2 phenotype through the PI3K/AKT signaling pathway. *Int Immunopharmacol*. 2022;102:108426.
50. Zhou X, Wu Y, Zhang Y, et al. Targeting α7 nicotinic acetylcholine receptor for modulating the neuroinflammation of dry eye disease via macrophages. *Invest Ophthalmol Vis Sci*. 2025;66:13.
51. Sweeney DF. Have silicone hydrogel lenses eliminated hypoxia? *Eye Contact Lens*. 2013;39:53–60.
52. Zhu S, Shan H, Li J, et al. Corrigendum: therapeutic potential of topical administration of acriflavine against hypoxia-inducible factors for corneal fibrosis. *Front Pharmacol*. 2023;14:1161682.
53. Meng YF, Pu Q, Dai SY, Ma Q, Li X, Zhu W. Nicotinamide mononucleotide alleviates hyperosmolarity-induced IL-17a

secretion and macrophage activation in corneal epithelial cells/macrophage co-culture system. *J Inflamm Res*. 2021;14:479–493.

54. Qu M, Wang Q, Bai X, et al. A gatekeeper sympathetic control of lacrimal tear secretion and dry eye onset through the NA-Adra1a-Ucp2 pathway. *Nat Commun*. 2025;16:5215.
55. Gubin D, Weinert D, Stefani O, Otsuka K, Borisenkov M, Cornelissen G. Wearables in chronomedicine and interpretation of circadian health. *Diagnostics (Basel)*. 2025;15:327.
56. Burgess HJ, Park M, Wyatt JK, Fogg LF. Home dim light melatonin onsets with measures of compliance in delayed sleep phase disorder. *J Sleep Res*. 2016;25:314–317.
57. Liu J, Si H, Huang D, et al. Mechanisms of extraorbital lacrimal gland aging in mice: an integrative analysis of the temporal transcriptome. *Invest Ophthalmol Vis Sci*. 2023;64:18.
58. Benjamin WJ, Rasmussen MA. Oxygen consumption of the superior cornea following eyelid closure. *Acta Ophthalmol (Copenh)*. 1988;66:309–312.
59. Davis C, Hackett P. Advances in the prevention and treatment of high altitude illness. *Emerg Med Clin North Am*. 2017;35:241–260.
60. Tanaka T, Kojima I, Ohse T, et al. Cobalt promotes angiogenesis via hypoxia-inducible factor and protects tubulointerstitium in the remnant kidney model. *Lab Invest*. 2005;85:1292–1307.
61. Lee YF, Yong DWW, Manotosh R. A review of contact lens-induced limbal stem cell deficiency. *Biology (Basel)*. 2023;12:327.
62. Eckle T, Bertazzo J, Khatua TN, et al. Circadian influences on myocardial ischemia-reperfusion injury and heart failure. *Circ Res*. 2024;134:675–694.
63. Young ME. The cardiac circadian clock: implications for cardiovascular disease and its treatment. *JACC Basic Transl Sci*. 2023;8:1613–1628.
64. Licastro E, Viscardi V, Cuomo O, et al. Timing matters: how daily rhythms affect remote ischemic postconditioning therapy for stroke [published online ahead of print September 11, 2025]. *Stroke*.
65. Mergenthaler P, Balami JS, Neuhaus AA, et al. Stroke in the time of circadian medicine. *Circ Res*. 2024;134:770–790.
66. Zhang L, Xiong W, Li N, et al. Estrogen stabilizes hypoxia-inducible factor 1α through G protein-coupled estrogen receptor 1 in eutopic endometrium of endometriosis. *Fertil Steril*. 2017;107:439–447.
67. Kondratov RV, Kondratova AA, Gorbacheva VY, Vykhovanets OV, Antoch MP. Early aging and age-related pathologies in mice deficient in BMAL1, the core component of the circadian clock. *Genes Dev*. 2006;20:1868–1873.
68. Imai T, Takimoto Y, Takeda N, Uno A, Inohara H, Shimada S. High-speed video-oculography for measuring three-dimensional rotation vectors of eye movements in mice. *PLoS One*. 2016;11:e0152307.